ANALYTICAL STUDY OF MIXING AND REACTING THREE-DIMENSIONAL SUPERSONIC COMBUSTOR FLOW FIELDS*

By A. J. Baker,**
Bell Aerospace Division of Textron

R. Clayton Rogers,
NASA Langley Research Center

and S. W. Zelazny
Bell Aerospace Division of Textron

SUMMARY

An analytical investigation is presented of mixing and reacting hydrogen jets injected from multiple orifices transverse and parallel to a supersonic airstream. The COMOC computer program, based upon a finite-element solution algorithm, was developed to solve the governing equations for three-dimensional, turbulent, reacting, boundary-region and confined flow fields. The computational results provide a three-dimensional description of the velocity, temperature, and species-concentration fields downstream of hydrogen injection. Detailed comparisons between cold-flow data and results of the computational analysis have established validity of the turbulent-mixing model based on the elementary mixing-length hypothesis. A method is established to initiate computations for reacting flow fields based upon cold-flow correlations and the appropriate experimental parameters of Mach number, injector spacing, and pressure ratio. Key analytical observations on mixing and combustion efficiency for reacting flows are presented and discussed.

INTRODUCTION

The hydrogen-fueled scramjet engine is a prominent candidate for propulsion of advanced hypersonic cruise vehicles. (See, for example, Becker and Kirkham (ref. 1) and Bushnell (ref. 2).) An airframe-integrated underbody engine configuration (figs. 1(a) and (b)) has been suggested (ref. 3), and design considerations are discussed by Henry and Anderson (ref. 4). Many alternative scramjet designs have been proposed by the U.S. Air Force, the U.S. Navy, and NASA. In all cases, however, fuel introduction typically consists of rows of circular, choked-flow fuel injector orifices mounted flush and

*This work was supported principally by NASA under Contracts NAS1-11214 and NAS1-13165.

**Visiting Professor, Old Dominion University.

normal to the combustor wall or in fins spanning the combustor inlet. (See fig. 1(c).) The various proposed component designs have largely emerged from laboratory experimentation wherein empirical relations have established a preliminary configuration. Detailed experimental parametric evaluations are then utilized to optimize design configuration.

The ability to analytically predict turbulent, mixing, and reacting three-dimensional flows, and hence avoid the more costly exclusively experimental approach, has been the long-range goal of rocket and ramjet designers for more than a decade. Three very difficult problems must yield to solution to attain this goal. First, a computational technique for solving the appropriate three-dimensional flow field with a predominant flow direction is required. Second, proper turbulent diffusion models must be selected or developed, since the accuracy of the predictive calculation is strictly dependent upon the adequacy of these models for combined laminar and turbulent diffusion of mass, momentum, and energy. Consequently, detailed baseline data characterizing the flow phenomena over a reasonably wide range of flow parameters must be obtained to confirm the validity of the theoretical modeling.

The objective of this investigation is to describe analytically the mixing and reaction of hydrogen in a supersonic airstream simulating the combustion of a scramjet engine. Current combustor design concepts (ref. 4) for scramjet engines employ fuel injection both from transverse wall injectors and from internal struts containing both parallel and transverse injection orifices. Therefore, the analytical characterization of both fuel injection modes is sought. In particular, the problem areas considered are illustrated in figure 2 for the mixing and reaction zones downstream of a row of transverse injection orifices (fig. 2(a)) and the parallel strut injectors (fig. 2(b)). Details of the mixing and reaction promoted by these distinct geometric configurations are computed by using a considerable extension of the exploratory theoretical studies documented in references 5, 6, and 7.

Experimental data for comparison with these analyses are provided from references 8, 9, 10, and 11. In references 8 and 9, detailed velocity and concentration measurements were made in a nonreacting, three-dimensional, hydrogen-air mixing region downstream of a row of laterally spaced circular orifices. The hydrogen was injected from the orifices, at various pressures, transverse to a turbulent Mach 4 air boundary-layer flow over a flat plate. In the experiments reported in reference 10, ambient-temperature hydrogen was injected at nominal equivalence ratios of 0.5 and 1.0 transverse to a hot supersonic test gas (vitiated air) from rows of circular orifices in opposite walls of a two-dimensional duct. Data measurements included static pressure distributions at the duct wall and pitot pressure and gas composition surveys at the duct exit, from which the reacted fraction of injected hydrogen was deduced. Additional reacting-flow data are available from the experimental investigation reported in reference 11,

where two distinct strut fuel injectors were tested in a hot supersonic duct flow. In the transverse injection strut, hydrogen was injected from orifices just downstream of a rearward-facing step. In the parallel configuration, hydrogen was injected parallel to the main flow from conical nozzles drilled at the base of the strut wedge. Data measurements were similar to those of the previously discussed hot-flow experimentation. Generated predictions are compared with select data sets from each of these experimental investigations.

Long-term support has been given to finite-element research in computational fluid mechanics by Bell Aerospace Division of Textron. Significant contributions were provided by W. T. Rushmore and J. A. Orzechowski.

SYMBOLS

a	boundary-condition coefficient
A	species; area
b	coefficient
B	species
c	coefficient
c_p	specific heat
C	species
C_f	skin friction
d	differential; orifice diameter
f	function of known argument
g	function of known argument
h	static enthalpy; duct height
H	stagnation enthalpy; hydrogen

i	index
$\hat{i},\hat{j},\hat{k}$	unit vectors of rectangular Cartesian coordinate system
k	thermal conductivity; constant
K	generalized diffusion coefficient; equilibrium constant
ℓ	differential operator; number; mixing length
L	characteristic length; differential operator
m	number
M	Mach number; number of finite elements
n	unit normal vector; number; nodes per element; dimensionality
N	nitrogen; composition matrix
N_{Pr}	Prandtl number
N_{Re}	Reynolds number
N_{Sc}	Schmidt number
O	oxygen
p	pressure
q	generalized dependent variable
q_r	dynamic pressure ratio
Q	generalized discretized dependent variable
R	domain of elliptic operator; universal gas constant

s	injector spacing
S	mass source term; finite-element assembly operator
T	temperature
u,U	velocity
W	molecular weight
x_i	rectangular Cartesian coordinate system
X	species mole fraction
Y	species mass fraction
β	pressure gradient parameter
γ	ratio of specific heats
∂R	closure of elliptically coupled solution domain
δ	boundary-layer thickness
Δ	increment
ϵ	kinematic eddy viscosity
η	mixing efficiency
κ	coefficient
λ	multiplier; turbulence sublayer constant
μ	viscosity
ρ	density
σ	integral kernel

τ integral kernel; wall shear

ϕ equivalence ratio, $\dfrac{(\rho u_1)_{jet}}{0.034(\rho u_1)_{air}}$

Φ functional

χ domain of initial-value operator

ω turbulence damping factor

Ω global solution domain

Superscripts:

e effective value

T matrix transpose

α species identification

$\hat{}$ unit vector

* approximate solution

Subscripts:

e local reference condition

i,j,k tensor indices

m mth subdomain

o initial

t stagnation or total

T turbulent

α	species identification
β	elemental species
∞	global reference condition

Notation:

$\{\}$	column matrix
$[\,]$	square matrix
$\cup$	union
$\cap$	intersection
$\sum$	summation
$\in$	belongs to

THEORETICAL DEVELOPMENT

Many researchers are now giving attention to numerical solution of three-dimensional parabolic and/or boundary-region flow fields. Most procedures employ a finite-difference solution algorithm for variously combined forms of the continuity, momentum, and energy equations. Note that the three-dimensional boundary-layer equations result from this parabolic set for flow fields wherein diffusion in one direction only is important and the corresponding pressure gradient is negligible. Several researchers have obtained solutions for the three-dimensional boundary-region flow of single-species fluids. Pal and Rubin (ref. 12) employ asymptotic expansions of the flow variables for laminar incompressible flow after transformation to modified stream function and vorticity. Results of extending the theory to a compressible perfect fluid in physical variables are reported by Cresci et al. (ref. 13), who used an extension of the numerical technique common to boundary-layer solutions. Extension to handle streamwise pressure gradients and refinement of the overall method are reported by Rubin and Lin (ref. 14). Caretto et al. (ref. 15) present a finite-difference algorithm for solution of three-dimensional boundary-region flows with extension to the "parabolic" Navier-Stokes equations. The results of computations for transitional internal flows in rectangular ducts are presented

by Curr et al. (ref. 16). Refinement of the overall procedure with particular attention to solution of the parabolic Navier-Stokes equations is given by Patankar and Spalding (ref. 17). The key feature of their theory is a procedure for splitting the pressure field computation such that a two-dimensional boundary-value problem results for pressure in the transverse plane coupled to an assumed uniform streamwise pressure gradient computed from global continuity. The latter step is similar to methods employed for computations in two-dimensional hydrodynamics (ref. 18).

Characterization of an n-species, three-dimensional boundary-region or parabolic flow field requires solution of (n - 1) species-continuity equations in addition to those previously mentioned. Caretto (ref. 15) and Patankar and Spalding (ref. 17) include results of a finite-difference solution of heat, mass, and momentum transfer in three-dimensional parabolic flows. Baker (ref. 19) presents a finite-element solution algorithm for multiple-species diffusion in supersonic, three-dimensional boundary-region flow. However, no general three-dimensional solution algorithm has been published which considers mixing and reacting three-dimensional confined flows.

The system of partial differential equations governing such three-dimensional, confined unidirectional flows of a compressible, reacting fluid is obtained as an approximation to the full three-dimensional Navier-Stokes equations. This approximation, now known as the "parabolic Navier-Stokes equations," describes steady, confined three-dimensional flows wherein (1) a predominant flow direction is uniformly discernible; (2) in this direction (only), diffusion processes are negligible compared with convection; and (3) no disturbances are propagated upstream antiparallel to this direction. The three-dimensional boundary-region equations are obtained as a subset of the parabolic Navier-Stokes equations with the single but significant assumption that a known pressure distribution is superimposed upon the flow field. The velocity vector lying on a three-dimensional Euclidean space spanned by a rectangular Cartesian coordinate system x_i is identified as

$$u_i \equiv u_1\hat{i} + u_2\hat{j} + u_3\hat{k} \tag{1}$$

For development of the governing equation system, assume that $\hat{i}$ is parallel to the predominant flow direction. Identify the two-dimensional vector differential operator

$$(\,)_{,k} \equiv \hat{j}(\,)_{,2} + \hat{k}(\,)_{,3} \tag{2}$$

where the comma identifies the gradient operator. In Cartesian tensor notation, with summation over 2 and 3 for repeated Latin subscripts, the parabolic Navier-Stokes equation system for a multiple-species, compressible, reacting flow takes the form

$$0 = (\rho u_i)_{,i} + (\rho u_1)_{,1} \tag{3}$$

$$\rho u_1 Y^{\alpha}_{,1} = \left(\frac{\mu^e}{N_{Sc}N_{Re}} Y^{\alpha}_{,k}\right)_{,k} - \rho u_k Y^{\alpha}_{,k} + S^{\alpha} \tag{4}$$

$$u_1 u_{j,1} = \left(\frac{\mu^e}{N_{Re}} u_{j,k}\right)_{,k} - u_k u_{j,k} - p_{,j} \tag{5}$$

$$\rho u_1 H_{,1} = \left(\frac{\mu^e}{N_{Re}N_{Pr}} H_{,k}\right)_{,k} - \rho u_k H_{,k} - \gamma M_{\infty}^2 \left[\frac{1 - N_{Pr}}{N_{Pr}} \frac{\mu^e}{2N_{Re}} \left(u_j^2\right)_{,k}\right]_{,k}$$

$$- \left(\frac{N_{Sc} - N_{Pr}}{N_{Sc}N_{Pr}} \frac{\mu^e}{N_{Re}} \sum h^{\alpha} Y^{\alpha}_{,k}\right)_{,k} \tag{6}$$

The variables appearing in equations (3) to (6) are nondimensionalized with respect to ρ_{∞}, U_{∞}, H_{∞}, and a length constant L, and have their usual interpretation in fluid mechanics. The Reynolds number N_{Re}, Prandtl number N_{Pr}, and Schmidt number N_{Sc} are defined for a combination of laminar and turbulent contributions as, for example,

$$\frac{\mu^e}{N_{Pr}} \equiv \frac{\mu}{N_{Pr}} + \frac{\rho\epsilon}{(N_{Pr})_T} \tag{7}$$

In equation (7), μ is the laminar viscosity, ϵ is the kinematic eddy viscosity, and the subscript T denotes a turbulent reference parameter. The stagnation enthalpy is defined in terms of species static enthalpies as

$$H \equiv \sum_{\alpha} h^{\alpha} Y^{\alpha} + \frac{1}{2} u_k^2 \tag{8}$$

The static enthalpy includes the heat of formation h_o^{α} of the species in its definition as

$$h^{\alpha} \equiv \int_{T_o}^{T} c_p^{\alpha}\, dT + h_o^{\alpha} \tag{9}$$

An equation of state is required to close the system. Assuming perfect-gas behavior for each species, from Dalton's law,

$$p = \rho R T \sum_{\alpha} \frac{Y^{\alpha}}{W^{\alpha}} \tag{10}$$

where R is the universal gas constant and W^{α} is the molecular weight of the αth species.

There are two approximate methods which may be effectively used to describe reacting hydrogen-oxygen-air systems. In the first case, assume that prototype scramjet combustors are adequately described by equilibrium combustion. The following reactions are operative:

$$\left.\begin{aligned} 2H + O &\rightleftharpoons H_2O \\ 2H &\rightleftharpoons H_2 \\ 2O &\rightleftharpoons O_2 \\ H + O &\rightleftharpoons OH \\ N_2 + 2O &\rightleftharpoons 2NO \end{aligned}\right\} \tag{11}$$

The equilibrium composition of the combustion byproducts is determined by applying the law of mass action (ref. 6) to each reaction defined in equations (11). This yields definition of a set of equilibrium constants K, which, for the simple reaction $nA + mB \rightleftharpoons \ell C$, are expressed in terms of species mole fraction X^{α} as

$$K \equiv \frac{\left[X^A\right]^n \left[X^B\right]^m}{\left[X^C\right]^{\ell}} \tag{12}$$

Solution of equation (11), coupled with equation (12) and conservation of total and elemental mass, yields an algebraic equation system for determination of the equilibrium composition of the system, of the form

$$\left[N_{\alpha\beta}\right]\left\langle X^{\alpha}\right\rangle = \left\langle \text{Constant} \right\rangle \tag{13}$$

In equation (13), the elements of the matrix [N] account for the distribution of the particular species mole fraction $\left\langle X^{\alpha}\right\rangle$ containing the βth elemental material, for example, O, H, and N.

Solution of the equilibrium temperature and species concentration requires an iterative solution to a nonlinear algebraic equation system. A considerably less expensive method (from the standpoint of computer time) may be employed to obtain an upper limit on the effects of heat release on the flow field development. The mole fractions of the dissociated species O and H are usually small compared with those of O_2 and H_2. Equations (11) may then be considerably simplified by assuming that the complete reaction

$$H_2 + \frac{1}{2} O_2 \rightarrow H_2O \tag{14}$$

is the only reaction that occurs. In this case all the H_2 reacts with the available O_2 to form H_2O. By describing the variation of specific heats with temperature through a polynomial relationship of the form $c_p \equiv a + bT + cT^2$, the temperature is solved explicitly in terms of the enthalpy and pressure without iteration.

For internal flows, characterized by boundary-layer thicknesses which are small in comparison with the overall internal duct dimension, the pressure distribution can be accurately approximated by inviscid flow solutions. However, in the alternate case where the flow is confined in a duct whose lateral dimension is not large with respect to the boundary-layer thickness, this approach is invalid. Here, boundary-layer development directly influences the pressure distribution within the duct, and an axial pressure gradient is induced by viscous effects. For these flows, a quasi-one-dimensional integral treatment of equations (3) and (5) has been suggested (refs. 17 and 20), wherein for steady flows, equations (3) and (5) are integrated across the duct transverse dimensions to obtain an equivalent expression written on mass-averaged dependent variables defined by

$$Q \equiv \frac{1}{\dot{m}A} \int_{A(x_1)} \rho u_1 q \, d\tau \tag{15}$$

In equation (15), $A(x_1)$ is the duct area, which may be a function of axial location x_1; $\dot{m}$ is the mass flow rate

$$\dot{m} \equiv \rho u_1 A \tag{16}$$

and q represents a generalized dependent variable which may be selectively streamwise velocity u_1, static temperature T, or density ρ. Taking the logarithmic differential of equation (16) gives

$$\frac{dA}{A} = \frac{d\dot{m}}{\dot{m}} - \frac{du_1}{u_1} - \frac{d\rho}{\rho} \tag{17}$$

The integral momentum equation (eq. (5)) implies

$$A \, dp + F \, dx_1 + u_1 \, d\dot{m} + \dot{m} \, du_1 = 0 \tag{18}$$

where F is the retarding force per unit length of duct exerted by viscous interaction of the confined flow with the wall. The equation of state for a perfect fluid of constant molecular weight may be logarithmically differentiated to yield

$$\frac{d\rho}{\rho} = \frac{dp}{p} - \frac{dT}{T} \tag{19}$$

Combining equations (15) to (19) yields an explicit relation for axial pressure gradient as

$$p_{,1} = \frac{-\frac{F}{A} - \frac{2u_1}{A}\dot{m}_{,1} + \frac{\dot{m}u}{A^2}A_{,1} - \frac{\dot{m}u_1}{AT}T_{,1}}{1 - \frac{\dot{m}u_1}{Ap}} \tag{20}$$

If an initial pressure level and the detailed flow field at a given station are known, equation (20) can be evaluated and integrated to yield downstream pressure levels. To achieve this, the friction force per unit duct length is related to the wall shear stress τ as

$$F \equiv \tau p \tag{21}$$

where p is the wetted perimeter of the duct. For the rectangular combustor geometries considered herein as bounded by symmetry planes,

$$\frac{F}{A} = \frac{\tau}{x_2^w} \tag{22}$$

where τ is evaluated as a function of the local velocity gradient at the wall (ref. 20) and x_2^w is the distance from the center plane of the duct to the wall.

Calculation of the change in mass flow rate with respect to axial distance requires a computational distinction between the actual mass flow $\dot{m}^r$ and the computed mass flow $\dot{m}^f$. The difference between $\dot{m}^r$ and $\dot{m}^f$ provides an estimate of the pressure and pressure gradient required to maintain conservation of mass. The rate of change of mass flow with respect to x_1 is defined as

$$\dot{m}_{,1} = \frac{\Delta\dot{m}}{\Delta x_1} \tag{23}$$

where

$$\Delta\dot{m} = \Delta\dot{m}^f - \Delta\dot{m}^r \tag{24}$$

and

$$\Delta\dot{m}^r = \dot{m}^r(x_1 + \Delta x_1) - \dot{m}^r(x_1) \tag{25a}$$

$$\Delta\dot{m}^f = \dot{m}^r(x_1) - \dot{m}^f(x_1) \tag{25b}$$

$$\Delta x_1 \equiv (x_1)_{new} - (x_1)_{old} \tag{26}$$

In equation (25a), $\Delta\dot{m}^r$ represents the mass flow increment which results from the mass addition, whereas $\Delta\dot{m}^f$ (eq. (25b)) represents the mass flow error obtained at the

upstream station x_1. Examination of equations (20) and (23) to (25) shows that use of equation (23) will always provide a pressure gradient which tends to make the computed and actual mass flow discrepancy decrease and hence models the physical flow.

For the analyses presented herein, flow-field turbulence has been modeled by means of an eddy-coefficient hypothesis. It should be noted that more sophisticated alternatives exist; their application to the problem class at hand will occur as the data base expands, as has occurred for modeling turbulence in two-dimensional and simple three-dimensional flows (refs. 21 and 22). The computer code implementing the finite-element algorithm for the equation system has been developed so that higher order turbulence models may be directly incorporated into the governing equation set and solution vectors. Elementary mixing-length theory (MLT) has proved very useful in characterizing the mixing of mass, momentum, and energy over a wide variety of flow conditions (ref. 23). Bearing this in mind, as well as the essential boundary-layer character of the considered flows, the baseline turbulent model was selected as the MLT and was employed to compute the evolutionary (downstream) development of all dependent variables. The success of more sophisticated turbulence modeling may then be assessed on a quantitative basis to evaluate explicitly any improvements at the expense of introducing additional empirical relationships and/or constants.

The MLT model is employed to compute the eddy diffusivities of momentum ϵ, mass $\epsilon(N_{Sc})_T^{-1}$, and thermal energy $\epsilon(N_{Pr})_T^{-1}$. Each is expressed in terms of the mixing length ℓ, the mean longitudinal velocity u_1, and distance normal to the wall x_2, according to the equation

$$-\overline{uv} \equiv \epsilon \frac{\partial u_1}{\partial x_2} = \ell^2 \left|u_{1,2}\right| u_{1,2} \tag{27}$$

The mixing length is defined as

$$\ell \equiv \begin{cases} kx_2\omega & (0 \leqq x_2 \leqq \lambda\delta/k) \\ \lambda\delta\omega & (x_2 > \lambda\delta/k) \end{cases}$$

where

k = 0.435

λ sublayer constant

δ boundary-layer thickness

x_2 coordinate normal to wall

The Van Driest damping coefficient is

$$\omega \equiv 1 - \exp\left(-\frac{\tilde{x}_2}{A}\right)$$

where

$\tilde{x}_2$ $\equiv \frac{\tilde{u}x_2}{\nu}$

$\tilde{u}$ friction velocity, $\sqrt{\tau/\rho}$

τ skin friction

ρ density at wall

ν kinematic viscosity

A $\equiv 23.5$

FINITE-ELEMENT SOLUTION ALGORITHM

The parabolic Navier-Stokes equation system and the three-dimensional boundary-region equation system excepting global continuity (eq. (3)) are uniformly constituted as initial boundary-value problems of mathematical physics. Each of the subject partial differential equations (eqs. (4) to (6)) is a special case of the general, second-order, nonlinear partial differential equation

$$L(q) \equiv \kappa\left[K(q)q_{,k}\right]_{,k} + f(q,q_{,i},x_i) + g(q,\chi) = 0 \tag{28}$$

where q is a generalized dependent variable identifiable with each computational dependent variable. In equation (28), f and g are specified functions of their arguments, χ is identified with x_1 for parabolic flows, and x_i are the coordinates for which second-order derivatives exist in the lead term. The finite-element solution algorithm is based upon the assumption that $L(q)$ is uniformly parabolic within a bounded open domain Ω; that is, the lead term in equation (28) is uniformly elliptic within its domain R, with closure ∂R, where

$$\Omega = R \times \left[\chi_o,\chi\right) \tag{29}$$

and $\chi_o \leqq \chi$. If equation (28) is uniformly parabolic, unique solutions for q are obtained upon specification of functional constraints on $\partial\Omega = \partial R \times \left[\chi_o,\chi\right)$ and an initial-condition specification on $R \cup \partial R \times \chi_o$. For constraints on $\partial\Omega$, the general form relates the function and its normal derivative everywhere on the closure ∂R as

$$\ell(q) \equiv a^{(1)}q(\bar{x}_i,\chi) + a^{(2)}Kq(\bar{x}_i,\chi)_{,k}n_k - a^{(3)} \equiv 0 \tag{30}$$

In equation (30), the $a^{(i)}(\bar{x}_i,\chi)$ are user-specified coefficients, the superscript bar notation constrains x_i to ∂R, and n_k is the local outward-pointing unit normal vector. For an initial distribution, assume that

$$q(x_i,\chi_o) \equiv q_o(x_i) \tag{31}$$

is given throughout $R \cup \partial R \times \chi_o$.

The finite-element solution algorithm is established for the equation system (28) to (31) by using the method of weighted residuals (MWR) formulated on a local basis. Since equation (28) is valid throughout Ω, it is valid within disjoint interior subdomains Ω_m described by $(x_i,\chi) \in R_m \times [\chi_o,\chi)$, called finite elements, wherein $\cup R_m = R$. An approximate solution for q within $R_m \times [\chi_o,\chi)$, called $q^*_m(x_i,\chi)$, is formed by expansion into a series solution of the form

$$q^*_m(x_i,\chi) \equiv \{\Phi(x_i)\}^T\{Q(\chi)\}_m \tag{32}$$

In equation (32), the functionals $\Phi_k(x_i)$ are subsets of a function set that is complete on R_m. The expansion coefficients $Q_k(\chi)$ represent the unknown χ-dependent values of $q^*_m(x_i,\chi)$ at specific locations interior to R_m and on the closure ∂R_m, called nodes of the finite-element discretization of R.

To establish the values taken by the expansion coefficients in equation (32), require that the local error in the approximate solution to both the differential equation $L(q^*_m)$ and the boundary-condition statement $\ell(q^*_m)$, for $\partial R_m \cap \partial R \neq 0$, be rendered orthogonal to the space of the approximation functions. By employing an algebraic multiplier λ, the resultant equation sets can be combined as

$$\underset{m}{S}\left[\int_{R_m} \{\Phi(x_i)\}\, L(q^*_m)\, d\tau - \lambda \int_{\partial R_m \cap \partial R} \{\Phi(x_i)\}\, \ell(q^*_m)\, d\sigma\right] \equiv \{0\} \tag{33}$$

where $\underset{m}{S}$ is the mapping function from the finite-element subspace R_m to the global domain R, commonly termed the assembly operator. The number of equations (33) prior to assembly is identical with the number of node points of the finite element R_m.

Equation (33) forms the basic operation of the finite-element solution algorithm and of the COMOC computer program. The lead term can be rearranged, and λ determined by means of a Green-Gauss theorem:

$$\int_{R_m} \{\Phi(x_i)\}\, \kappa\left[Kq^*_{m,k}\right]_{,k} d\tau = \kappa \oint_{\partial R_m} \{\Phi(x_i)\}\, Kq^*_{m,k} n_k\, d\sigma - \kappa \int_{R_m} \{\Phi(x_i)\}_{,k} Kq^*_{m,k}\, d\tau \tag{34}$$

For $\partial R \cap \partial R_m$ nonvanishing (eq. (34)), the corresponding segment of the closed-surface integral will cancel the boundary-condition contribution (eq. (33)) by identifying $\lambda a^{(2)}$ with κ of equation (28). The contributions to the closed-surface integral (eq. (34)), where $\partial R_m \cap \partial R = 0$, can be made to vanish (ref. 6). When equations (30) to (34) are combined, the globally assembled finite-element solution algorithm for the representative partial differential equation system becomes

$$\underset{m}{S}\left[-\kappa \int_{R_m} \{\Phi\}_{,k} K q^*_{m,k} d\tau + \int_{R_m} \{\Phi\}(f^*_m + g^*_m) d\tau \right.$$

$$\left. - \kappa \int_{\partial R_m \cap \partial R} \{\Phi\}\left(a^{(1)}_m q^*_m - a^{(3)}_m\right) d\sigma \right] = \{0\} \tag{35}$$

The rank of the global equation system (eq. (35)) is identical with the total number of node points on $R \cup \partial R$ for which the dependent variable requires solution. Equation (35) is a first-order, ordinary differential system, and the matrix structure is sparse and banded. Solution of the ordinary differential equation system is obtained by using a predictor-corrector finite-difference numerical integration algorithm (ref. 6).

A solution algorithm is required for the continuity equation, which is retained as equation (3) for boundary-region flows. Since equation (3) is an initial-value problem on ρu_2 as a function of x_2, with x_1 and x_3 appearing as parameters, the approximation function need span only the transverse coordinate direction as

$$(\rho u_2)^*_m = \{\Phi(x_2)\}^T \{\rho V(x_1, x_3)\}_m \tag{36}$$

The matrix elements of $\{\rho V\}$ are nodal values of ρu^*_2; their functional dependence requires solution of equation (3) along lines (x_1, x_3) equal a constant. Since equation (3) exists in standard form as an ordinary differential equation, direct numerical quadrature yields the required solution at node points of the discretization.

COMOC COMPUTER PROGRAM

The COMOC computer program system is being developed to transmit the rapid theoretical progress in finite-element solution methodology into a viable numerical solution capability. In the course of generating this general-purpose system, several variants of COMOC have been developed for specific problem classes, including transient thermal analysis and the two-dimensional Navier-Stokes equations as well as the three-dimensional boundary-region equations. The present operational variant of COMOC is capable of solving each of these problem classes and has been extended to include the parabolic Navier-Stokes equation system. An on-line restart feature allows the user to

switch between boundary-region and parabolic Navier-Stokes systems according to the requirements of the problem at hand. Generated solutions determine the three-dimensional distribution of all dependent variables and solution parameters for flow of a viscous, heat-conducting, multiple-species, compressible fluid including combustion. The flow may be external or confined, subsonic or supersonic, laminar and/or turbulent, and can contain up to nine or more distinct species in frozen composition or undergoing equilibrium or complete chemical reaction for a hydrogen-oxygen-air system.

The finite-element solution algorithm is utilized to cast the original initial-valued, elliptic boundary-value problems into large-order systems of purely initial-value problems. The program then integrates the discretized equivalent of the governing equation system in the direction parallel to the predominant flow. Initial distributions of all dependent variables may be arbitrarily specified, and boundary constraints for each can be specified by the user on arbitrarily disjoint segments of the solution domain closure. The solutions for each dependent variable, and all computed parameters, are established at node points lying on a specifiably nonregular, computational lattice formed by plane triangulation of the elliptic portion of the solution domain. Each of the computational triangles is spanned by a linear approximation function used for all independent and dependent variables as well as each solution parameter.

The COMOC system is built upon the macrostructure illustrated in figure 3. The main executive routine allocates core by means of a variable dimensioning scheme based upon the total degrees of freedom of the global problem. The size of the largest problem that can be solved is thus limited only by the available core of the computer in use. The precise mix between number of dependent variables (and parameters) and fineness of the discretization is user-specifiable and widely variable. The input module serves its standard function for all arrays of dependent variables, parameters, and geometric coordinates. The discretization module forms the finite-element discretization of the elliptic solution domain and evaluates all required finite-element nonstandard matrices and standard-matrix multipliers. The initialization module computes the remaining initial parametric data required to start the solution. The integration module constitutes the primary execution sequence of problem solution. It utilizes a highly stable, predictor-corrector integration algorithm for the column vector of unknowns of the solution. Calls to auxiliary routines for parameter evaluation (viscosity, Prandtl number, source terms, combustion parameters, etc.) as specified functions of dependent and/or independent variables are governed by the integration module. The user has considerable latitude to adapt COMOC to the specifics of his particular problem by directly inserting readily written subroutines to compute special forms of these parameters. The output module is similarly addressed from the integration sequence and serves its standard function via a highly automated array display algorithm. COMOC can execute distinct problems in sequence and contains an automatic restart capability to continue solutions.

EXPERIMENTAL DATA

The presented theoretical model has been applied to the prediction of mixing and reaction of hydrogen in a supersonic flow field simulating a scramjet combustor. Two hydrogen injector arrangements were considered: (1) a row of circular orifices on the wall that inject hydrogen transverse to the main flow and (2) strut injectors in both a parallel and a transverse injection configuration. Before discussing the comparisons between theory and experiment, it is appropriate to review the source and nature of the experimental data.

Nonreacting Flow

In the experimental investigation reported in references 8 and 9, hydrogen was injected from multiple, laterally disposed circular orifices transverse to a nominal Mach 4 airstream over a flat plate. The turbulent boundary layer was approximately 3 injector diameters thick at the injector station (without injection). Tests were conducted for ratios q_r of jet dynamic pressure to main-stream dynamic pressure of 0.5, 1.0, and 1.5. Each of these conditions was sufficient to maintain the injectors in a choked condition. For each value of q_r, data were obtained at stations $x_1/d = 7$, 30, 60, and 120 downstream of the point of injection, and for individual injector spacings s/d of ∞ (single jet), 12.5, and 6.25. At each test condition (q_r and s/d) and at each station x_1/d, the hydrogen-air mixing region was mapped by making a vertical survey directly downstream of the center jet and horizontal surveys at three elevations above the plate surface. In each survey, the measurements consisted of a two-dimensional mapping of local pitot and static pressures and the molar concentration of hydrogen. From these data, profiles of velocity, mass flux, and hydrogen mass fraction were determined. Details of the probe design, measurements, and data reduction may be found in references 8 and 9.

Reacting Flow

An experimental investigation of the reaction of hydrogen in a hot supersonic test gas flowing through a two-dimensional duct is reported in reference 10. The hydrogen was injected at ambient temperature and transverse to the main flow from rows of circular orifices in opposite walls of the duct. The test gas, a simulation of supersonic airflow at altitude, was supplied by a burner in which hydrogen, oxygen, and air mixtures were reacted in such proportions that the resulting oxygen concentration of the mixture was 21 percent by volume (vitiated air). Nominal stagnation conditions of the test gas were 2200 K and 2.7 MN/m^2 at a Mach number of 2.7. Details of the burner operation are given in references 24 and 25. Several injector configurations differing in the number, size, and spacing of the distinct injectors were tested at nominal equivalence ratios

ϕ of 0.5 and 1.0. An equivalence ratio of unity signifies a stoichiometric mixture; less than unity indicates fuel-lean operation. Data measurements consist of two-dimensional distributions of wall static pressure, bulk heat transfer to the water-cooled wall, and surveys of pitot pressure and gas composition across the horizontal center plane of the duct exit.

Strut Injector Tests

Additional reacting-flow data have been obtained (ref. 11) for parallel and perpendicular (to the main flow) injection of hydrogen from strut injectors spanning the combustor. The objective of these tests was to determine the flow fields produced by simple strut injectors and to compare these results with theory based on a one-dimensional analysis and empirical mixing models. For these tests a hot-gas simulation of Mach 7 flight was made. The test gas was supplied by the hydrogen-oxygen-air burner mentioned in the previous section. For the perpendicular injection strut, the hydrogen was injected from equally spaced, choked orifices drilled just downstream of a modest rearward-facing step located at the maximum strut thickness. The parallel injection strut employed five equally spaced conical nozzles in the base of strut. Aerodynamically, both struts were simple 6° half-angle wedges that spanned the width of the duct. Data acquisition consisted of distributions of duct-wall static pressure and surveys of pitot pressure and gas composition on the horizontal center plane at the duct exit. Details on the operation of the hydrogen-oxygen-air burner, the probe measurements, and data reduction can be found in references 24 and 25.

NUMERICAL RESULTS

The objective of this study is to formulate and evaluate a theoretical model for describing the complex three-dimensional phenomena associated with scramjet combustion of hydrogen-air systems at supersonic speeds. It has been hypothesized that the finite-element solution algorithm for the governing three-dimensional equation systems, coupled with elementary mixing-length turbulence modeling and constant Schmidt and Prandtl numbers, represents an adequate first step toward the desired goal. The numerical results presented in this section verify this supposition and its limitations and are presented in three categories. First, it is essential that the accuracy and convergence character of the finite-element solution algorithm be numerically assessed and verified. Results which provide this required information are presented for lower dimensional problems involving laminar and turbulent flows. Second, it is necessary to validate the hypothesized turbulence model by correlation of predictions with experimental test data over a wide range of design parameters. Finally, for the theoretical model to be viable as a design tool, it is necessary to establish a means for extending the initialization pro-

cedures to hot flow and to obtain correlation with experimental data for practical combustor configurations. The numerical results of these three distinct phases are correspondingly discussed in this section.

Accuracy and Convergence

As noted in the Introduction, the conventional two- and three-dimensional boundary-layer equations represent a dimensionally degenerate subset of the equation systems under study for application to supersonic combustion devices. With the boundary-condition versatility that is intrinsic in the finite-element solution technique, it is possible to establish a two-dimensional solution within the three-dimensional solution domain and solve the corresponding supersonic boundary-layer problem without alteration to the code. The generated results may then be evaluated for accuracy and convergence by comparison with solutions produced by finite-difference techniques and with a similarity solution for constant specific heat. The check case corresponds to a nominal Mach 5, laminar, two-dimensional, air boundary-layer flow over an adiabatic wall in a favorable pressure gradient. With the assumption of constant specific heat, the flow is isoenergetic and it is necessary only to solve the x_1 momentum equation and the continuity equation. The initial distribution for longitudinal velocity u_1 is established from the similar solution for $\beta = 0.5$ and $S = 0$ of reference 26. The initial distribution for u_2 is obtained iteratively, and Sutherland's law is employed to compute viscosity.

The test case is initialized at $x_1 = 0.03$ m downstream from the leading edge. The boundary-layer thickness at this station δ_o is 0.0039 m, the local Mach number M_e is 3.77, the Reynolds number N_{Re} is 0.83×10^5 per meter, and the adiabatic wall temperature T_w is 1000 K. Shown in figure 4 are the COMOC computed distributions of skin friction, local free-stream Mach number, and boundary-layer thickness for the case of constant specific heat. These were obtained with two uniform finite-element discretizations corresponding to four and eight elements spanning the initial boundary-layer thickness. The input static pressure distribution $p_e(x_1)$ is also presented for reference. The boundary-layer thickness has increased more than fourfold within the solution domain. Only small differences, on the order of about 2 percent, exist between the two solutions, the finer discretization producing a slightly larger skin friction and smaller local Mach number. Superimposed in figure 4 for comparison purposes are the results for the similar solution (ref. 26) and a 20-zone finite-difference solution obtained with the Von Mises coordinate transformation. Agreement among the four solutions is excellent (within 2 percent) for skin friction. The similar solution for M_e lies between the COMOC and finite-difference solutions, and overall agreement is within ±3 percent.

Shown in figure 5 are computed velocity profiles at $x_1/\delta_o = 22.7$, which is about midway through the presented solution domain. Shown for reference is the initial longi-

tudinal velocity profile with the node locations of the four-element discretization superimposed. Both COMOC solutions produce u_1 distributions that are slightly more concave upward in the midregion in comparison with the similar or finite-difference solution. The eight-element COMOC solution lies closer to the similar solution in the region where the two finite-element solutions differ. The finite-difference solution lies appreciably below both the COMOC and similar solutions near the free stream. The computed transverse velocities, which are also plotted in figure 5, show only slight differences between the two discretization solutions. The trends of the COMOC solutions are in excellent agreement with the established procedures; unfortunately, since each method of solution is distinctly numerical, no absolute accuracy assessment is established. However, for an incompressible boundary-layer flow, absolute accuracy and convergence rates for the finite-element solution have been established to be close to theoretically predicted values (ref. 27).

This check case establishes an accuracy assessment of solution of three-dimensional boundary-region equations. A similar evaluation of the parabolic Navier-Stokes equation system has been obtained for three different channel flow configurations. Figure 6 summarizes the results for a nonreacting subsonic flow to evaluate the ability of the pressure solution algorithm (eq. (20)) to compute a constant streamwise gradient. For the fully developed channel flow, streamwise velocity and the pressure gradient are computationally maintained to within ±2.5 percent of their initial values. The computations for developing channel flow correctly predicted the downstream distance required to attain fully developed flow; that is, COMOC predicted that the flow was fully developed at $x_1/h = 33$ (compared with $x_1/h = 30$ reported in ref. 28). A similar evaluation was performed to assess channel flow computations with heat addition. Conditions were selected such that in the initial portion of the flow, reaction of hot air with cold hydrogen induces a favorable pressure gradient (heat addition in subsonic flow). However, after the available oxygen supply is exhausted, the continued mixing of the cold hydrogen with the heated combustion products produces an overall temperature drop and, hence, an adverse pressure gradient. The computational results are summarized in figure 7; the trends are observed to have been correctly captured by COMOC while maintaining conservation of mass to within ±1.0 percent.

Correlation With Cold-Flow Data

Early design studies of a prototype injection scheme for a supersonic combustor (ref. 3) considered the transverse injection of hydrogen as the primary means of fuel introduction into the airstream. Consequently, as discussed in the previous section, detailed concentration, velocity, and pressure measurements were made for an appropriately scaled experimental configuration (shown in fig. 8). As a function of the dynamic pressure ratio, the sonically injected hydrogen penetrates the turbulent supersonic air

boundary layer to a certain distance and in the process turns downstream as illustrated. This complex turning phenomenon exerts considerable influence on the initial mixing of the injectant with the main flow. Furthermore, and of equal importance, the subsequent hydrogen distributions (fig. 8) are convected downstream by the main flow while the hydrogen diffuses in the plane transverse to this direction. For multiple-injector configurations, the concentration patterns merge as illustrated; thus, a three-dimensional effect in addition to mixing and reaction is imposed.

To verify a viable theoretical model, it is necessary to evaluate the appropriateness of the hypothesized mixing-length turbulence model. The detailed experimental results of Rogers (refs. 8 and 9) for the configuration illustrated in figure 8 provide the necessary data base for comparison of predictions. Initial conditions for the predictions were established from these data, and the downstream station at $x_1/d = 30$ was selected as the initialization station. The original raw data consist of a single vertical traverse and three lateral traverses on the transverse plane at several x_1 stations. The measured hydrogen mass fraction distributions appear of Gaussian shape; however, the symmetry plane of the data was variously displaced from the geometric symmetry plane. Although the entire flow field could be computed numerically, the strong appearance of a data symmetry plane suggested establishment of a corresponding computational solution domain. Therefore, a cubic spline interpolation program was applied to the raw data program to establish the x_3/d location of the data symmetry plane via a minimization criteria on the wings of the Gaussian-type distributions. The spline package then interpolated the raw data for hydrogen mass fraction and u_1 and output the evaluation of the interpolation polynominals at node points of the finite-element discretization of the transverse plane. A representative case of the spline-computed distributions of hydrogen mass fraction is shown in figure 9 in comparison with the spread and context of the experimental data.

Although plots of the form of figure 9 are geometrically aesthetic, the transition from the initial distributions and significant detail on solution accuracy and trends are better obtained by plotting concentration profiles $(x_2/d$ against $Y^H)$ along planes $x_3/d = \text{Constant}$ at each longitudinal station for which data measurements exist. The parameters evaluated experimentally include dynamic pressure ratio q_r and discrete injector spacing s/d for a Mach 4 flow in an unconfined geometry:

Discrete injector spacing, s/d	Dynamic pressure ratio, q_r		
	0.5	1.0	1.5
∞	✓	✓	✓
12.5	✓	✓	✓
6.25	✓		

Computational evaluation of the influence of all conditions has been made with the three-dimensional boundary-region variant of COMOC and a nonuniform discretization of the transverse plane (R in eq. (29)) into 100 finite elements. As the study progressed, computational evaluations were also made of the influence of a nonzero transverse velocity component u_3 as well as the magnitude of the sublayer constant λ in the mixing-length model.

Presented in figures 10 and 11 are the computed distributions of hydrogen mass fraction on planes $x_3/d = \text{Constant}$ at downstream stations $x_1/d = 60$ and 120 for the test conditions $q_r = 1.0$ and $s/d = 12.5$. In addition, the "universally" accepted value $\lambda = 0.09$ of the mixing-length model (eq. (27)) was employed, and zero transverse velocity was assumed. In all cases, the symbols represent data or data spread corresponding to "best symmetry" at the particular location. The solid curves denote the computed distributions, and each dashed curve corresponds to the initial distribution faired through the data at $x_1/d = 30$, which is presented for reference. At the first downstream station (fig. 10), agreement of the computational predictions with data is generally acceptable everywhere except near the plate surface for the first two profiles corresponding to the plane of symmetry and the next adjacent plane, $x_3/d = 0$ and 1.0. Agreement with data is degraded somewhat at the far downstream station (fig. 11), with predictions missing data points both near the wall and near the peak for the first two representations. Out of the core region of the jet, agreement with data remains quite good, however.

The correlation between predictions and data for the test case shown in figures 10 and 11 is a significant improvement over previous attempts (ref. 5). For good agreement in the centroidal region of the hydrogen jet, it is necessary that the maximum hydrogen concentration remain off the wall. Therefore, either from three-dimensional effects or a complex turbulence interaction between the jet and the wall, there is a mechanism in play capable of resisting the unidirectional trend of maximum diffusion to the wall. It has been hypothesized, as a result of the initial studies (ref. 5), that the existence of a mass flux transverse to the main flow direction and along the plate surface might account for the experimentally measured centroidal peak. Such a transverse mass flux could be initiated by the displacement effect of the sonic hydrogen jet issuing transverse to the main flow, since in such an interaction problem, the jet appears to the mainstream flow in many ways similar to an impervious body. Consequently, immediately downstream of the transverse jet, there must exist an approximately spheroidal fixed recirculation region near the wall, and a transverse mass flux would be required to alleviate a localized low-pressure area just downstream of this bubble.

This hypothesis was computationally evaluated for the test case just described by imposition of a small negative, transverse velocity distribution beneath the measured hydrogen concentration maximum at $x_1/d = 30$. The magnitude and vertical extent of the imposed transverse velocity on the symmetry center plane are shown in figure 12(a).

Figure 12(b) illustrates the lateral spread of the imposed transverse velocity distribution. For reference purposes, figure 12(a) also illustrates the longitudinal velocity distribution u_1 on the center plane at the initial station $x_1/d = 30$ as well as the predicted distributions at the remaining downstream data stations.

The influence of the imposed transverse velocity on the predicted distributions of hydrogen mass fraction at the two downstream data stations is shown in figures 13 and 14. The selected u_3 velocity distribution is observed not to alter significantly the mass fraction distributions above the peak but does substantially promote the existence of a local off-plate maximum in the centroidal region at $x_1/d = 60$. However, by the time the last data station is reached (fig. 14), the imposed transverse velocity distribution has been essentially dissipated (see fig. 12), and the computed distributions of hydrogen mass fraction in the centroidal region are noted to revert to the form of the maximum existing at the plate surface. It can be concluded, therefore, that transverse mass flow is probably of influence in the near region downstream of the point of injection. However, there is as yet some undetermined mechanism for maintaining the off-axis peak in the mass fraction distribution at stations far downstream. This undoubtedly points to some deficiency in the turbulent mixing model for this configuration and serves to emphasize the need for a more comprehensive theoretical model for describing three-dimensional turbulent mass mixing. For example, an approach based on turbulent kinetic energy and dissipation function might prove valuable.

After some computational experimentation, it was determined that all data could be correlated with superior accuracy by changing the value of the mixing-model sublayer coefficient λ to 0.07 and keeping $(N_{Pr})_T = 0.7$. (It should be noted that essentially the same hydrogen distributions could be predicted using the combination of $\lambda = 0.09$ and $(N_{Pr})_T = 0.90$. The difference between solutions obtained using $\lambda = 0.07$ and $(N_{Pr})_T = 0.7$ would be primarily in the velocity field.) Although this differs from the universally accepted value, it is certainly not unreasonable to expect this value to change somewhat because of the three-dimensional character of the problem being studied. The effect of λ on predicted distributions of hydrogen mass fraction is shown in figures 15 and 16 for the test case $q_r = 1.0$ and $s/d = 12.5$. The previous good agreement obtained at station $x_1/d = 60$ (fig. 3) has not been degraded and has actually been improved away from the core region. More importantly, at $x_1/d = 120$, a distinct improvement in agreement with the data for all profiles is indicated. Since the purpose of the present study is not a detailed development of a mixing model per se but evaluation of the analytical concept, the value of $\lambda = 0.07$ is used uniformly in all subsequent data correlations for both cold- and hot-flow configurations.

The influence of injectant dynamic pressure ratio q_r on the validity of the hypothesized mixing-length turbulence model has been evaluated for the test cases $s/d = 12.5$,

$\lambda = 0.07$, and $u_3 = 0$ at $q_r = 0.5$, 1.0, and 1.5. A summary of the results is presented in figure 17, which shows the comparison between predictions and data on the symmetry center plane $x_3/d = 0$ and at the lateral plane $x_3/d = 2.0$. By and large, agreement with data is consistent except for the low-pressure case ($q_r = 0.5$ on the symmetry plane), where overdiffusion is predicted. The trend of these results might have been anticipated in that the test case at the lowest dynamic pressure ratio corresponds to a weak jet dominated by near-wall effects. Imposition of a transverse velocity field u_3 might enhance agreement. This has not been verified, however, since low dynamic pressure ratios are of marginal practical interest.

The influence of spacing between discrete ejectors s/d has been computationally evaluated for $q_r = 1.0$ and $s/d = 12.5$ and ∞. Although more data exist for $q_r = 0.5$, the results of this comparison are liable to be inconclusive on the basis of the relatively poorer agreement seen in figure 17. Computed distributions of hydrogen mass fraction are shown in figure 18 in comparison with data for the symmetry center plane $x_3/d = 0$ and one other plane ($x_3/d = 2.0$ for $s/d = 12.5$ and $x_3/d = 2.5$ for $s/d = \infty$). The values $\lambda = 0.07$ and $u_3 = 0$ were retained for this comparison, and agreement of the predictions with data on the symmetry plane is observed to be consistent with previous experience. Somewhat poorer agreement exists off the symmetry plane for the single jet ($s/d = \infty$). This result might be expected, as three-dimensional diffusion effects are probably more dominant for the single jet, since it diffuses into a doubly unbounded domain. All multiple-jet configurations are expanding into only a singly unbounded domain downstream of merged interaction.

As with any multidimensional computations in compressible viscous fluid mechanics, it is important to establish a quantitative accuracy assessment. For the cold-flow configuration studied and reported herein, an accuracy measure of the adequacy of the employed discretization is possible by determining the conservation properties of the solution. For the cold mixing case, the species-continuity equation for hydrogen mass fraction can be written in explicit conservation form. Integrating this equation over a three-dimensional control volume and using Gauss' theorem (ref. 5) determines that the total hydrogen mass flow, that is, $\rho u_1 Y^H$, would be rigorously conserved by an analytic solution. COMOC evaluates this parameter at each output station by using linear finite-element approximation functionals for each variable and performing the integrations analytically. (Thus, the order of accuracy of the evaluation is consistent with that of the solution of the partial differential equations.)

For the test conditions $q_r = 1.0$, $s/d = 12.5$, and $u_3 = 0$, with $\lambda = 0.07$ (see figs. 15 and 16), a monotonically increasing loss of hydrogen mass flow with increasing distance downstream was computed; at $x_1/d = 120$, the computed loss equaled 8.8 percent of the mass flow computed at station $x_1/d = 30$. The 100-element standard nonuniform discretization was refined by a factor of 2 in each coordinate direction to produce

400 finite elements spanning R (see fig. 19, diagonals omitted), and the computation was repeated on $30 \leqq x_1/d \leqq 60$. Over this interval, the coarse discretization yielded a computed 5-percent loss in hydrogen mass flow. The fine discretization produced a modest variation in computed hydrogen mass flow over the initial interval, with a $1\frac{1}{2}$-percent net loss computed by $x_1/d = 60$. The resulting detailed differences in computed distributions of hydrogen mass fraction are shown in figure 20. Above the peak and outside the core region, differences are undiscernible on the scale of the plots. Within the core region, the maximum difference in computed hydrogen levels is less than 8 percent, which compares favorably with the 10- to 20-percent spread of the "best symmetry" data. The computational expense of these comparison solutions differed by over an order of magnitude. On an IBM 360/65, using no out-of-core devices for either case, the CPU time of the 100-element solution was about 250 seconds; on the same interval, the 400-element solution required 2600 seconds! Two parts constitute this increase (see ref. 6): a factor of about 4, due to the fact that the element DO loops in COMOC were 4 times longer, and a multiplicative factor of about 2, due to increased solution stiffness resulting from the refined grid itself. The ability of coarse finite-element discretizations, using low-order functionals, to preserve adequate engineering solution accuracy appears a distinct feature of the algorithm.

From these extensive correlations with data and the comprehensive numerical experimentation, it appears that the mixing-length turbulence model coupled with the finite-element solution of the three-dimensional boundary-region equation system provides an adequately accurate diagnostic tool for three-dimensional mixing of cold hydrogen injected into a supersonic turbulent boundary layer for dynamic pressure ratios q_r greater than 0.5 and for multiple jet configurations. Hence, the results discussed in these two sections give sufficient basis to pursue the computations detailed in the next section.

Extension to Hot-Flow and Combustor Correlations

A distinct feature of the three-dimensional boundary-region and parabolic Navier-Stokes equation systems is the capability to obtain a three-dimensional solution while marching in one coordinate direction. Elimination of the requirement for a downstream boundary condition is particularly important. For the subject mixing and combustion studies, however, the corresponding penalty is that an accurate initial condition is required to model adequately the complex near-injection flow field under study. In the previous section, the computations took advantage of detailed experimental profiles for the establishment of initial conditions. In the more general case, and in particular for hot-flow cases with combustion, detailed distributions of initial conditions are specifically unavailable, and a theoretical device for establishing the starting point of the solutions is required. Flow fields involving the parallel injection of dissimilar fluids present no dif-

ficulty, since smooth transitions occur and boundary-layer and shear-layer concepts are appropriate. However, for transverse injection, this is not the case, and some alternative means is required.

In anticipation of this need, a task in the early phases of the study was to evaluate the concept of a numerical "virtual source" as a means for eliminating the requirement for detailed initial conditions (ref. 5). Injection of a jet from an orifice in a plate transverse to a supersonic airstream has been the subject of a number of investigations. The important correlating parameter appears to be dynamic pressure ratio q_r. Most experimental data are for large values of q_r, for which the jet has sufficient momentum to penetrate the boundary layer and produce a complicated separation region and bow shock ahead of the jet. However, for the present cases, q_r ranges between 0.5 and 1.5, and a significant part of the jet remains within the turbulent boundary layer. Hence, mixing is initiated immediately downstream of injection. From these considerations, a theoretical model was proposed for establishing a barrel-shock—Mach disk hypothesis for turning of the transverse jet parallel to the main flow (see fig. 21). An analysis based on one-dimensional considerations was developed to characterize the jet turning. The important parameters in the model are dynamic pressure ratio q_r and free-stream Mach number M_∞, and the output is injectant momentum and flow area. Details of the model are presented in reference 5.

The validation of the concept of the virtual source as an initial-condition generator was accomplished by using the detailed cold-flow experimental data discussed in the previous section. Shown in figure 22 is the initial condition velocity surface, u_1 vs. (x_2,x_3), corresponding to a transverse cold hydrogen jet embedded (within the depression in the velocity surface) within the turbulent boundary-layer profile at $q_r = 1.0$. The detailed predicted distribution of hydrogen mass fraction are shown in figures 23 and 24 for the virtual-source simulation of the standard test case $(q_r = 1.0$ and $s/d = 12.5)$. For these computations, transverse velocity u_3 was assumed zero and $\lambda = 0.07$ in the turbulence model. Even after marching only 30 diameters downstream from the point of injection, agreement between the predictions and the data (fig. 23) is admirable, especially in the centroidal region, where there is an excellent prediction of an off-plate peak. At the final station $x_1/d = 120$ (fig. 24), agreement between the virtual-source simulation and data is excellent, being essentially identical with the results starting with data at $x_1/d = 30$ (fig. 11).

Shown in figure 25 is an alternative method for presenting these data which will be extended to the hot-flow comparisons. This figure presents the peak hydrogen concentration as a function of distance downstream. The agreement with data is excellent in the range $30 \leq x_1/d \leq 120$. The disagreement at $x_1/d = 7$ is not serious in light of the further downstream agreement; the indicated data point may well be significantly in error. Shown also in figure 25 are the trajectories of the peak hydrogen concentration above the

plate x_2/d and the lateral spread of the jet determined at the x_3/d coordinate where the local hydrogen concentration equals 10 percent of the local maximum. Observe that the local peak of the elevation trajectory sinks to the plate surface downstream of $x_1/d = 60$, as was observed for the multitudinous cold-flow data. The agreement of lateral spreading rate with data is excellent.

At the lower right in figure 25 is a computation of mixing efficiency η, defined as the fraction of hydrogen, integrated over the flow cross-sectional area at a given station, that would react if complete reaction with the available oxygen were to occur. This parameter has been used for correlating cold-flow data (ref. 9) and is readily computed by COMOC as an output parameter by means of the integration techniques utilized for measuring hydrogen mass flow. Hence, figures 23 to 25 demonstrate that the virtual-source concept of transverse hydrogen injection for the cold-flow configuration effectively simulates the injection phenomenon.

It is therefore hypothesized that the virtual-source concept is appropriate for combustion studies as well, and the experimental verification of this hypothesis is sought. As a first step, it is appropriate to measure the influence of combustion on the virtual-source cold-flow configuration. Shown also in figure 25 are computations carried out to $x_1/d = 30$ for the cold-flow simulation, but combustion of the hydrogen is now allowed to occur according to the complete-reaction hypothesis (eq. (14)). Note that the trajectory of maximum hydrogen mass fraction lies considerably above that for the cold-flow, nonreacting configuration. However, on the basis of mixing efficiency η, there is very little difference in overall mixing between the cold reacting and nonreacting cases.

The cold-flow problem is of marginal interest, however, since the average equivalence ratio of the cold-flow configuration ($\phi = 0.04$) lies well below the design level for a practical combustor. Note that equivalence ratio is defined (ref. 11) strictly in terms of the global mass flows of hydrogen and air. For stoichiometric combustion, $\phi = 1$; for fuel-lean operation, ϕ is less than 1. It is coincidental that the cold-flow virtual-source configuration can be thermodynamically altered (only) to correspond to conditions similar to test point 4 of reference 10. To simulate the test configuration, the cold flow was computationally vitiated by imposing an arbitrary uniform background hydrogen concentration (of 1 percent) and augmenting the oxygen level of the base flow such that the corresponding composition of the computational test gas simulates the hot (wet) air used for the experiment. The total temperature of the computational simulation was approximately 2000 K; the corresponding mass flow of cold hydrogen for the vitiated virtual source yielded $\phi = 0.4$, in comparison with $\phi = 0.5$ for the experiment. Shown in figure 25 are the trajectory of maximum hydrogen mass fraction, the elevation trajectory, and the lateral spreading rate for the vitiated virtual-source simulation of the test con-

figuration. Note that the elevation trajectory of the hot-flow configuration follows very closely the cold-flow data, a result possibly of the cold-wall ($T_w \equiv 0.5T_t$) boundary condition used for the computational simulation. It may also reflect the somewhat lessened lateral spreading rate for the vitiated reacting case, as shown in figure 25. Mixing efficiency was not computed for this vitiated combustion case. However, equivalence ratio, as a node point parameter, can be computed at any point in the solution domain. At the far right of the mixing-efficiency curve in figure 25, the experimentally determined range of equivalence ratio for test point 4 (ref. 10) is compared with the computed values. The presented computational values are in qualitative agreement with the experimental extremums on the center plane at the duct exit.

Of greatest practical importance, recent thinking on design of scramjet combustors hypothesizes that, depending upon flight Mach number, two fuel injection modes will be required. For example, an experimental model of a strut injector system (fig. 26) is currently under construction at Langley Research Center for evaluation of combustor performance as a function of injection mode. Design of this device was augmented by an earlier experimental program intended to evaluate the essential character of the two distinctly different injection modes proposed for this type of combustor (ref. 11). Sketches of the perpendicular and parallel injection struts that are associated with current design technology are shown in figure 27. In each case, given nearby is a virtual-source simulation of the proposed injection mode showing the location of the discrete injectors as well as the orientation of the virtual source within the computational domain. In the lower half of figure 27, an exploded view of the virtual-source simulation for the perpendicular injection mode is shown. The parallel injector corresponds to coaxial injection; its computational source domain is also shown in figure 27.

Velocity surface distributions for longitudinal velocity u_1 calculated for the virtual-source simulation of each injector configuration are shown in figures 28 and 29. Note that for the perpendicular injection strut (fig. 28), the cold hydrogen is embedded in a subsonic jet indicated by the severe depression in the velocity surface. This depression rapidly vanishes, as shown in the surface plot at the downstream station. Conversely, for the parallel injection mode (fig. 29), the simulation requires a supersonic hydrogen jet embedded within the air boundary-layer flow, hence the local velocity peak. This peak, likewise, is completely dissipated by the time the flow has proceeded downstream. To model this combustor, which employed a combustion duct with a modestly expanding cross-sectional area, the measured experimental pressure distribution was used for the computations, since COMOC is not yet operational with coordinate stretching functions in three dimensions.

Shown in figure 30 is the trajectory of the maximum hydrogen concentration as a function of injection mode for the experimental results reported in reference 11. Note

indeed that the perpendicular injection mode promotes much stronger mixing and hence produces a combustion process that proceeds considerably more rapidly than that corresponding to the parallel injection mode. Also plotted in figure 30 are the pressure distributions used for the computations, as well as the computed distribution of equivalence ratio on the center plane at $x_1/d = 150$ across one-half of a jet. Note that for the parallel injection mode, the range of computed equivalence ratio is twice that of the perpendicular case, in qualitative agreement with the data ranges from reference 11. Furthermore, the experimental evaluation of the differences in the flame shape for the two injection modes (ref. 11) with respect to apparent mixing rate is in agreement with the maximum hydrogen trajectories computed by the virtual-source simulation.

Hence, the analytical predictions are certainly not contrary to the available experimental information; more positively, they appear to be in essential agreement with the experimentally determined trends. Refinement of the theoretical model is certainly required, but the crucial confirmative results are at hand. The greatly detailed information available from the computational solutions may encourage the experimentalist to utilize the analytical capability to guide the design of future experiments. In this manner, important and relevant experimental data crucial to the ultimate verification of the validity of the analytical approach can be obtained. The availability of a computational and theoretical model that closely simulates the actual experimental configuration may thus enhance the overall value of the combustor design program in terms of information gained per unit expenditure of dollars and/or man hours. For example, when domain discretizations involving about 100 triangular finite elements were used, the parallel-strut test required only 1000 seconds of CPU time on an IBM 360/65 to run to $x_1/d = 200$. The perpendicular-strut test, with its much stronger mixing (and hence a stiffer differential equation system), required only 1500 seconds of CPU time to run to $x_1/d = 150$. Operation of the COMOC program is highly automated, and the same error criterion was used for both tests. An experienced user can prepare an entirely new data deck in about an hour. Execution of each test case, requiring evaluation of about 15 parameters and dependent variables at each node point of the discretization of R and at each downstream computational station, required about 340 000 bytes of rapid-access core in the computer. The next generation of computer hardware will significantly reduce present constraints with regard to both core requirements and CPU time.

CONCLUDING REMARKS

An analytical investigation has been presented on the turbulent mixing and reaction of hydrogen jets injected from multiple orifices transverse and parallel to a supersonic airstream. The proposed three-dimensional differential equation systems were solved by means of a finite-element algorithm in concert with a turbulent-mixing model based

on the elementary mixing-length hypothesis. The computational results have provided three-dimensional descriptions of the velocity, temperature, and species-concentration fields downstream of injection for geometries appropriate in practical combustor designs. Detailed comparisons between the predicted results and available experimental data have verified the validity of the analytical model and its ability to computationally simulate the experimental configuration with high fidelity. Thus, it appears that the newly emerged computational "laboratory" may well both supplement and supplant the experimental evaluation of prototype designs and, in particular, may facilitate detailed parametric studies.

REFERENCES

1. Becker, John V.; and Kirkham, Frank S.: Hypersonic Transports. Vehicle Technology for Civil Aviation – The Seventies and Beyond, NASA SP-292, 1971, pp. 429-445.

2. Bushnell, Dennis M.: Hypersonic Airplane Aerodynamic Technology. Vehicle Technology for Civil Aviation – The Seventies and Beyond, NASA SP-292, 1971, pp. 63-84.

3. Henry, John R.; and Beach, H. Lee: Hypersonic Air-Breathing Propulsion Systems. Vehicle Technology for Civil Aviation – The Seventies and Beyond, NASA SP-292, 1971, pp. 157-177.

4. Henry, John R.; and Anderson, Griffin Y.: Design Considerations for the Airframe-Integrated Scramjet. NASA TM X-2895, 1973.

5. Baker, A. J.; and Zelazny, S. W.: A Theoretical Study of Mixing Downstream of Transverse Injection Into a Supersonic Boundary Layer. NASA CR-112254, 1972.

6. Baker, A. J.; and Zelazny, S. W.: COMOC: Three-Dimensional Boundary Region Variant. Theoretical Manual and User's Guide. NASA CR-132450, 1974.

7. Orzechowski, J. A.; and Baker, A. J.: COMOC: Three-Dimensional Boundary Region Variant. Programmer's Manual. NASA CR-132449, 1974.

8. Rogers, R. Clayton: A Study of the Mixing of Hydrogen Injected Normal to a Supersonic Airstream. NASA TN D-6114, 1971.

9. Rogers, R. Clayton: Mixing of Hydrogen Injected From Multiple Injectors Normal to a Supersonic Airstream. NASA TN D-6476, 1971.

10. Rogers, R. C.; and Eggers, J. M.: Supersonic Combustion of Hydrogen Injected Perpendicular to a Ducted Vitiated Airstream. AIAA Paper No. 73-1322, Nov. 1973.

11. Anderson, Griffin Y.; and Gooderum, Paul B.: Exploratory Tests of Two Strut Fuel Injectors for Supersonic Combustion. NASA TN D-7581, 1974.

12. Pal, Alexander; and Rubin, Stanley G.: Viscous Flow Along a Corner. Part I. Asymptotic Features of the Corner Layer Equations. AFOSR-69-1225TR, U.S. Air Force, May 1969. (Available from DDC as AD 693 630.)

13. Cresci, R. J.; Rubin, S. G.; Nardo, C. T.; and Lin, T. C.: Hypersonic Interaction Along a Rectangular Corner. AIAA J., vol. 7, no. 12, Dec. 1969, pp. 2241-2246.

14. Rubin, Stanley G.; and Lin, Tony C.: A Numerical Method for Three-Dimensional Viscous Flow: Application to the Hypersonic Leading Edge. J. Comput. Phys., vol. 9, no. 2, Apr. 1972, pp. 339-364.

15. Caretto, L. S.; Curr, R. M.; and Spalding, D. B.: Two Numerical Methods for Three-Dimensional Boundary Layers. Comput. Methods Appl. Mech. & Eng., vol. 1, no. 1, June 1972, pp. 39-57.

16. Curr, R. M.; Sharma, Devraj; and Tatchell, D. G.: Numerical Predictions of Some Three-Dimensional Boundary Layers in Ducts. Comput. Methods Appl. Mech. & Eng., vol. 1, no. 2, Aug. 1972, pp. 143-158.

17. Patankar, S. V.; and Spalding, D. B.: A Calculation Procedure for Heat, Mass and Momentum Transfer in Three-Dimensional Parabolic Flows. Int. J. Heat & Mass Transfer, vol. 15, no. 10, Oct. 1972, pp. 1787-1806.

18. Amsden, Anthony A.; and Harlow, Francis H.: The SMAC Method: A Numerical Technique for Calculating Incompressible Fluid Flows. LA-4370, Los Alamos Sci. Lab., Univ. of California, Feb. 17, 1970.

19. Baker, A. J.: Finite Element Solution Theory for Three-Dimensional Boundary Flows. Comput. Methods Appl. Mech. & Eng., vol. 4, no. 3, Nov. 1974, pp. 367-386.

20. Patankar, S. V.; and Spalding, D. B.: Heat and Mass Transfer in Boundary Layers. Second ed. Int. Textbook Co. Ltd. (London), c.1970.

21. Free Turbulent Shear Flows. Volume I – Conference Proceedings. NASA SP-321, 1973.

22. Wheeler, A. J.; and Johnston, J. P.: An Assessment of Three-Dimensional Turbulent Boundary Layer Prediction Methods. Trans. ASME, Ser. I: J. Fluids Eng., vol. 95, no. 3, Sept. 1973, pp. 415-421.

23. Launder, B. E.; and Spalding, D. B.: Lectures in Mathematical Models of Turbulence. Academic Press, Inc., 1972.

24. Russin, William Roger: Performance of a Hydrogen Burner To Simulate Air Entering Scramjet Combustors. NASA TN D-7567, 1974.

25. Eggers, James M.: Composition Surveys of Test Gas Produced by a Hydrogen-Oxygen-Air Burner. NASA TM X-71964, 1974.

26. Christian, James W.; Hankey, Wilbur L.; and Petty, James S.: Similar Solutions of the Attached and Separated Compressible Laminar Boundary Layer With Heat Transfer and Pressure Gradient. ARL 70-0023, U.S. Air Force, Feb. 1970. (Available from DDC as AD 705 581.)

27. Popinski, Z.; and Baker, A. J.: An Implicit Finite Element Algorithm for the Boundary Layer Equations. J. Comp. Phys. (To be published, 1975).

28. Schlichting, Hermann (J. Kestin, transl.): Boundary-Layer Theory. Sixth ed. McGraw-Hill Book Co., Inc., 1968.

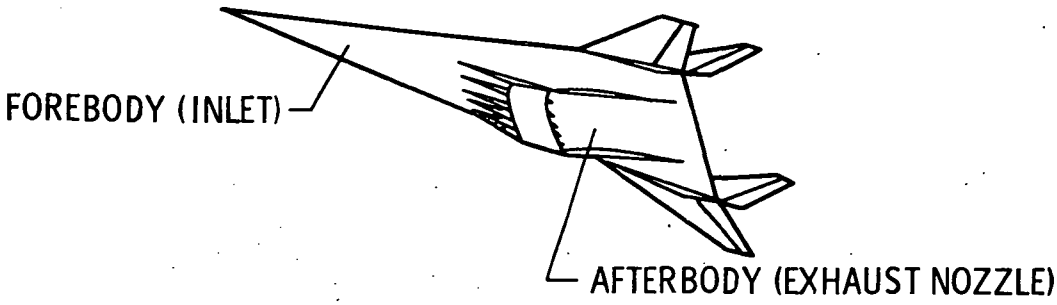

(a) Isometric view.

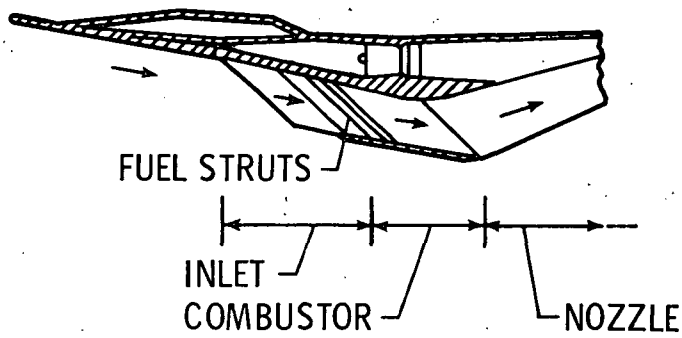

(b) Schematic of hypersonic propulsion system – scramjet operation above Mach 3.

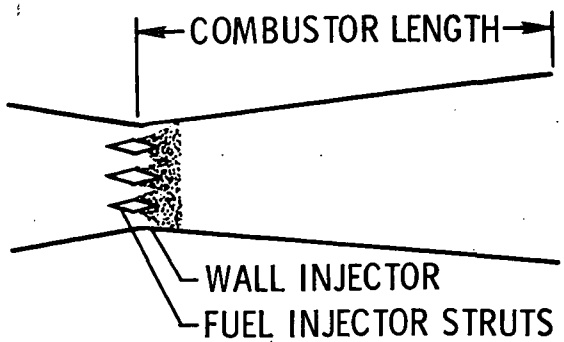

(c) Combustor length with in-stream fuel injection.

Figure 1.- NASA hypersonic research airplane.

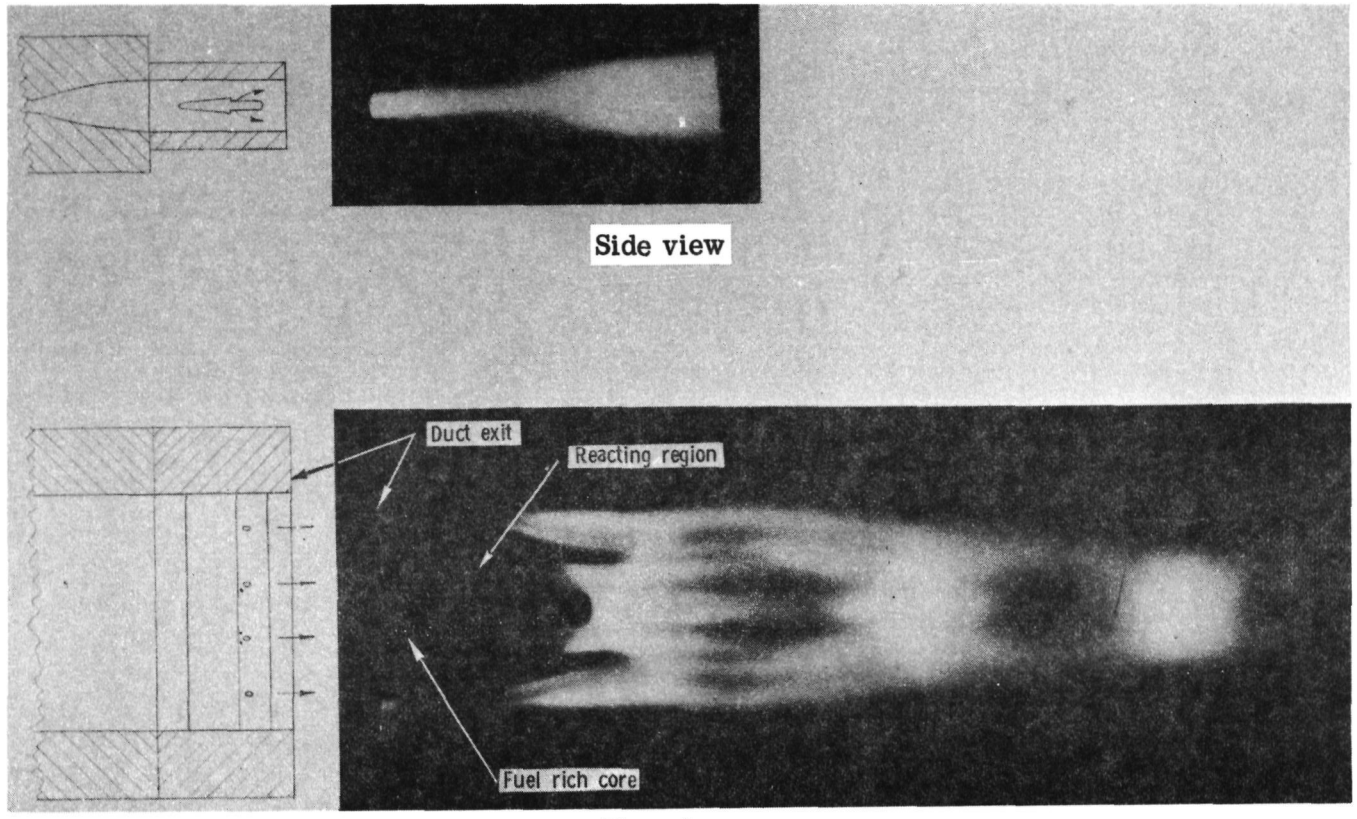

L-74-1011

(a) Perpendicular strut.

Figure 2.- Flame photographs of injection struts in short duct.

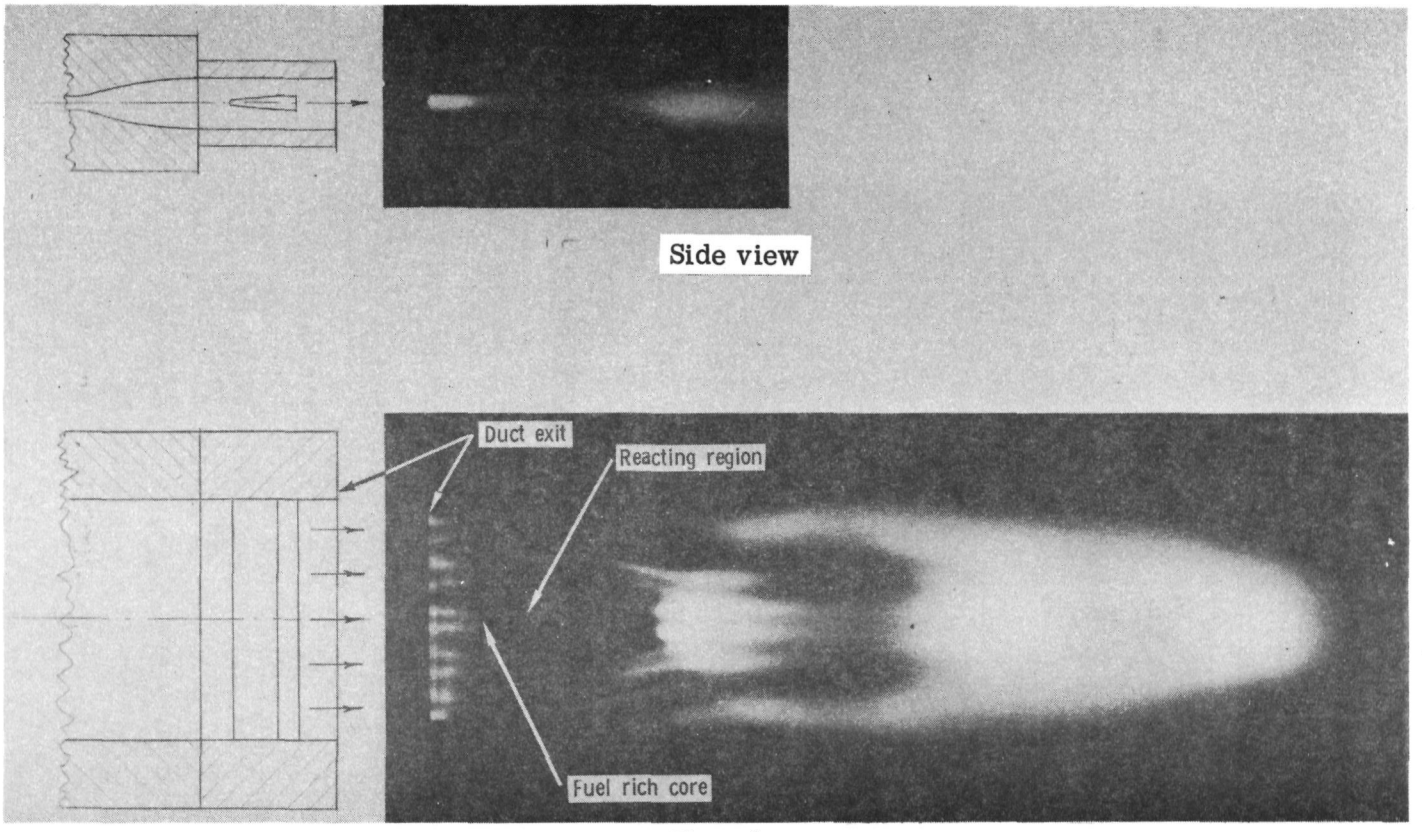

(b) Parallel strut.

Figure 2.- Concluded.

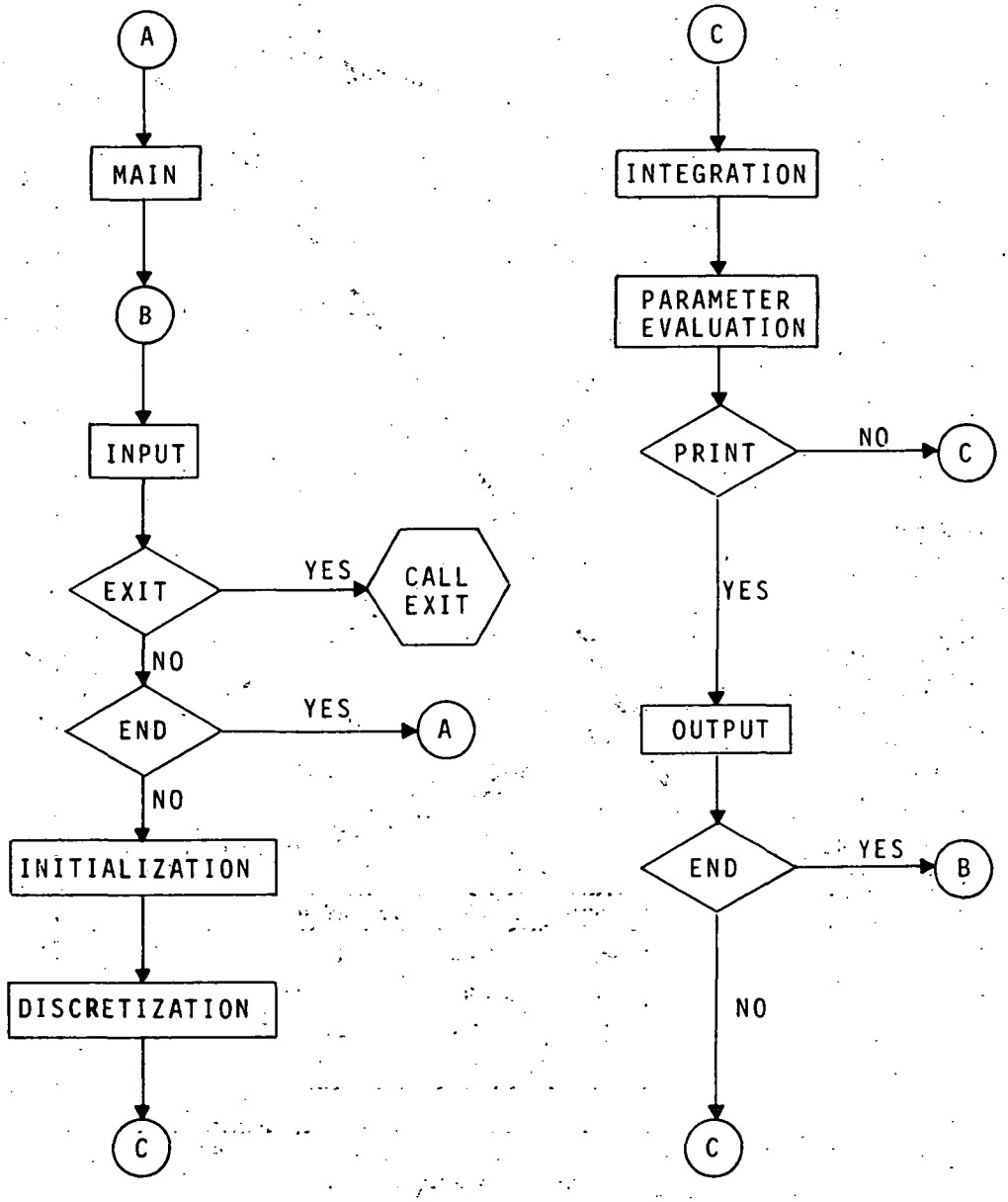

Figure 3.- COMOC macrostructure.

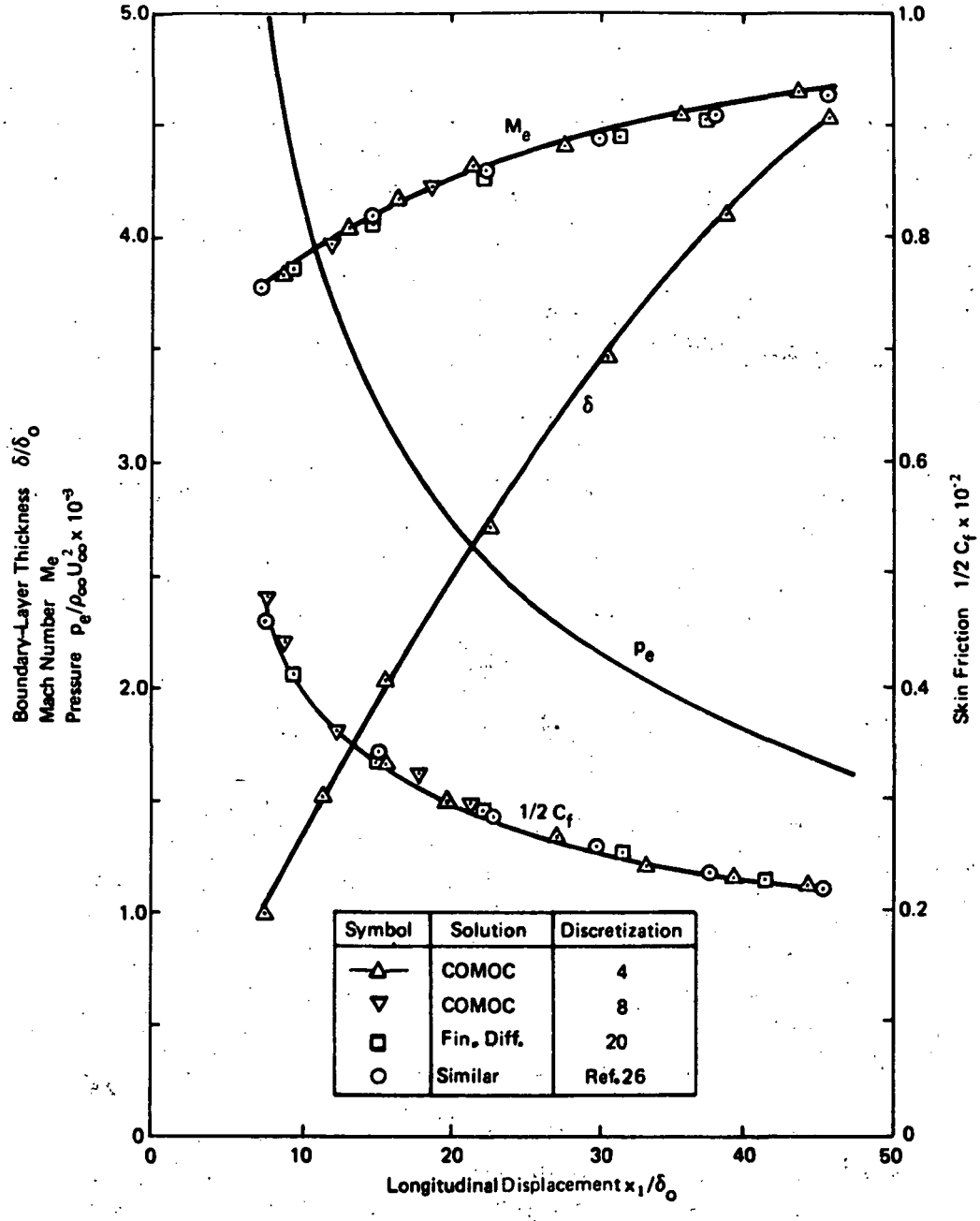

Figure 4.- Computed supersonic boundary-layer parameters. M = 5; $N_{Re} = 0.83 \times 10^5$ per meter; $\beta = 0.5$.

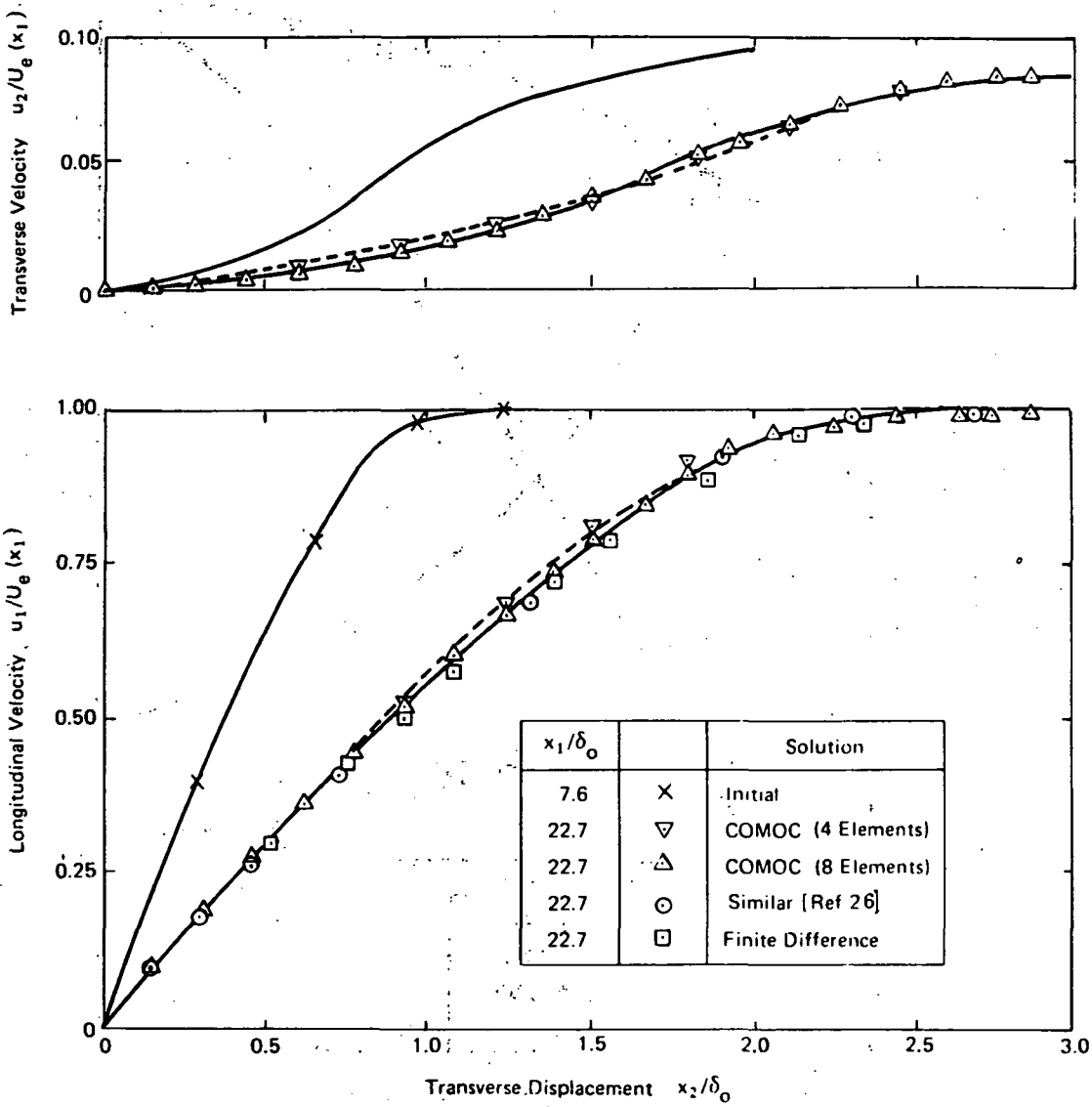

Figure 5.- Computed supersonic boundary-layer velocity profiles. M = 5; $N_{Re} = 0.83 \times 10^5$ per meter; $\beta = 0.5$.

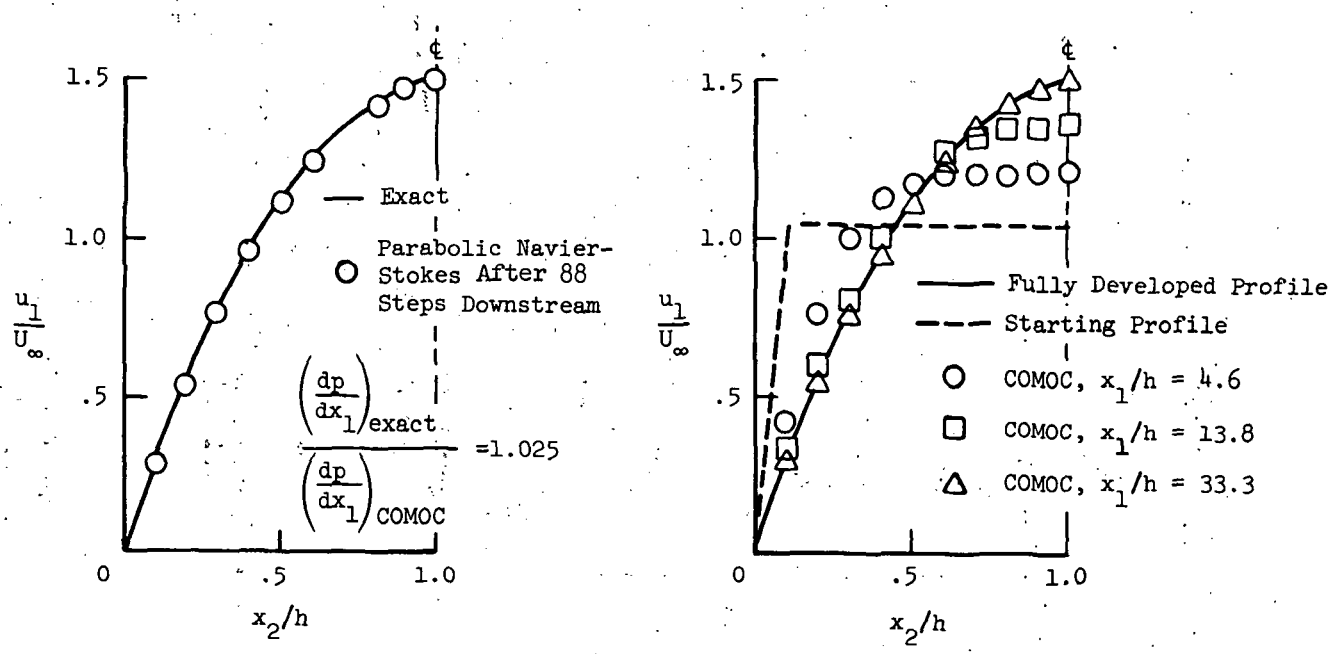

(a) Fully developed.

(b) Developing.

Figure 6.- Channel flow solutions computed with the parabolic Navier-Stokes equations.

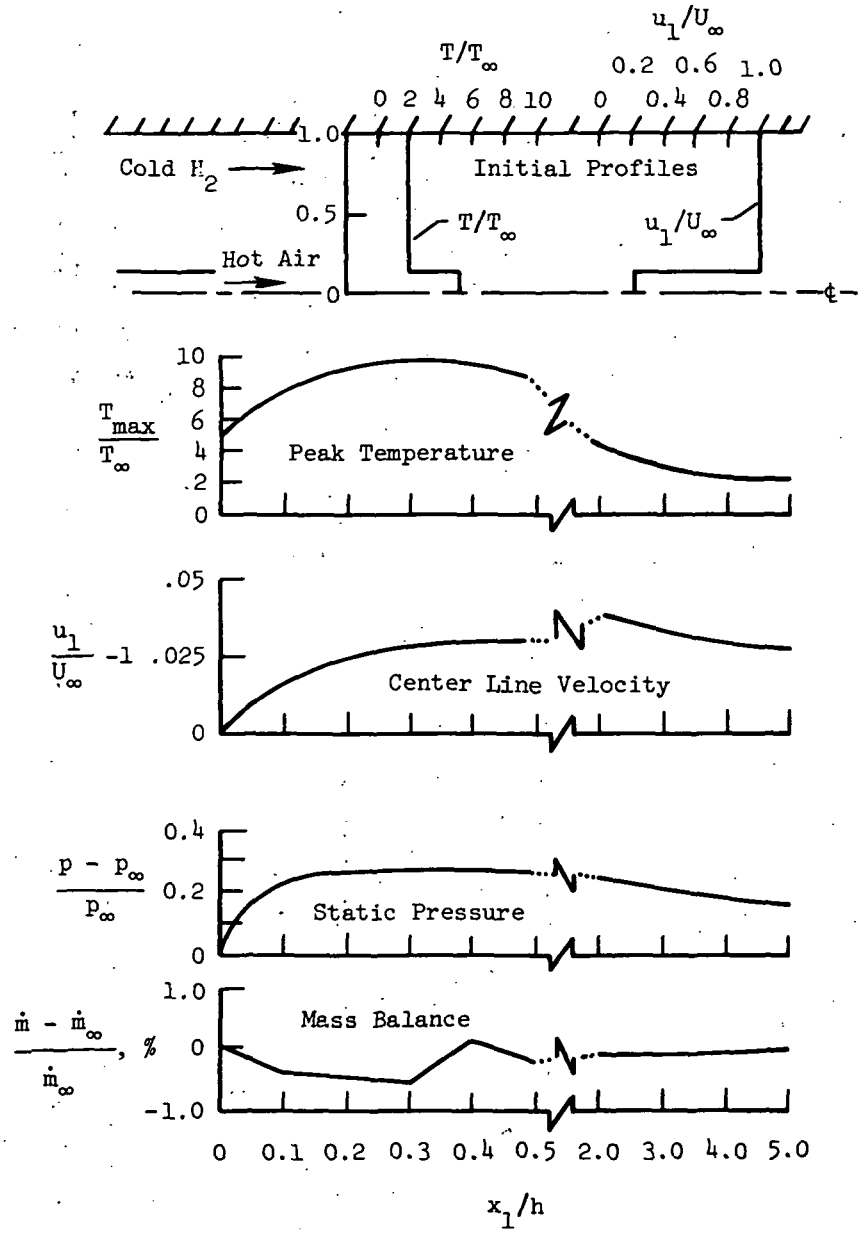

Figure 7.- Mixing and reacting channel flow. T_∞ = 400 K; U_∞ = 305 m/sec; h = 0.15 m.

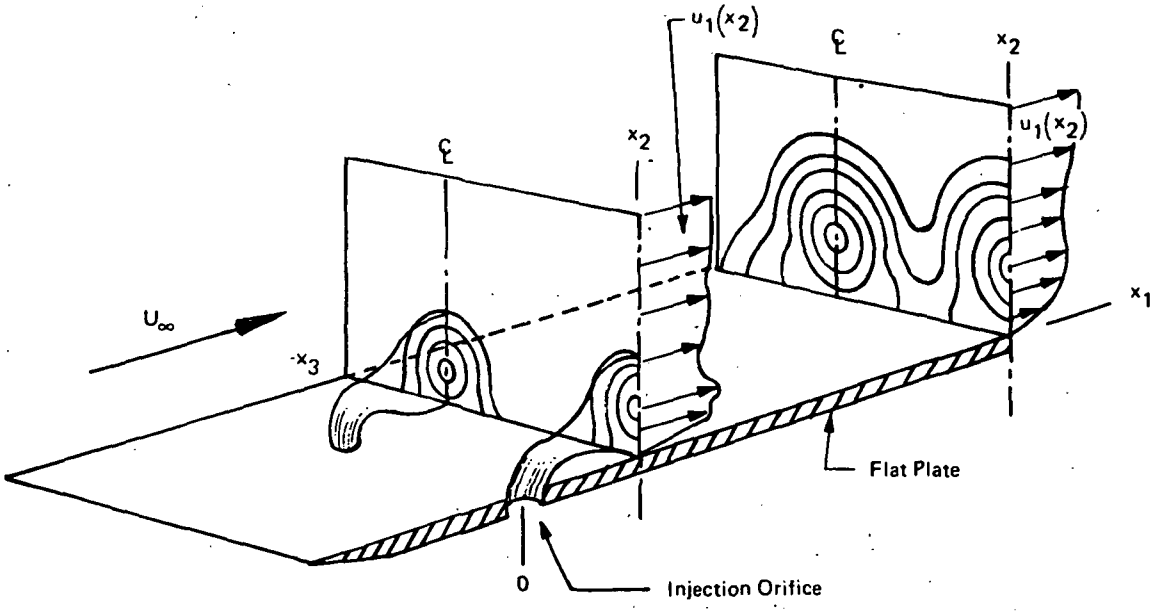

Figure 8.- Three-dimensional flow field downstream of transverse injection from discrete orifices.

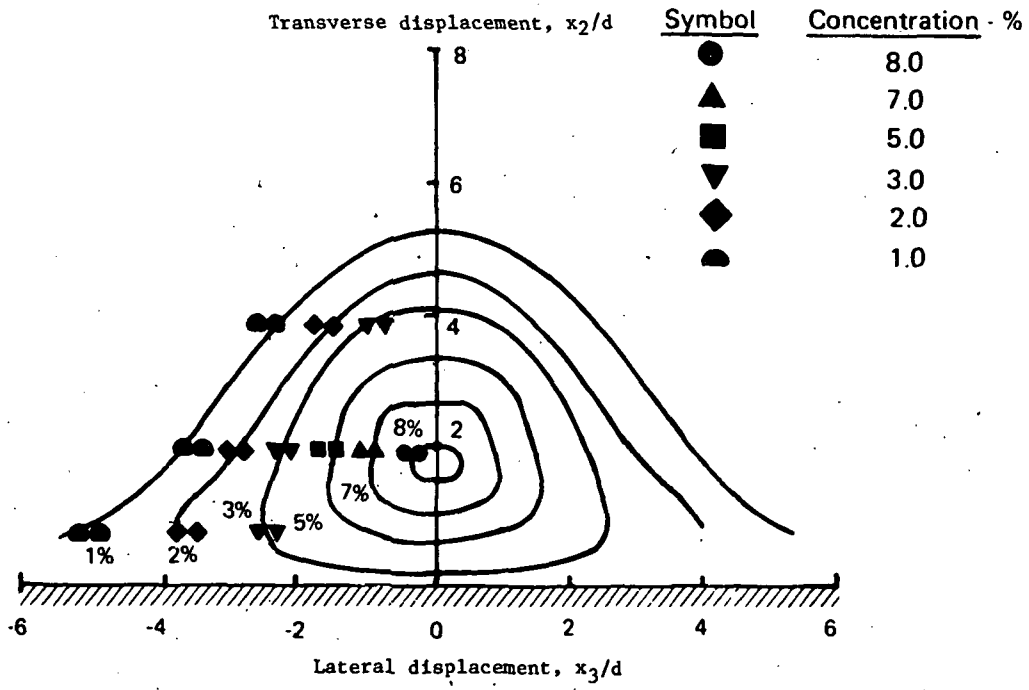

Figure 9.- Cubic-spline interpolated contours of hydrogen mass fraction. $q_r = 1.0$; $x_1/d = 30$; $s/d = \infty$. (Symbols are "best symmetry" fit for data of Rogers (ref. 8).)

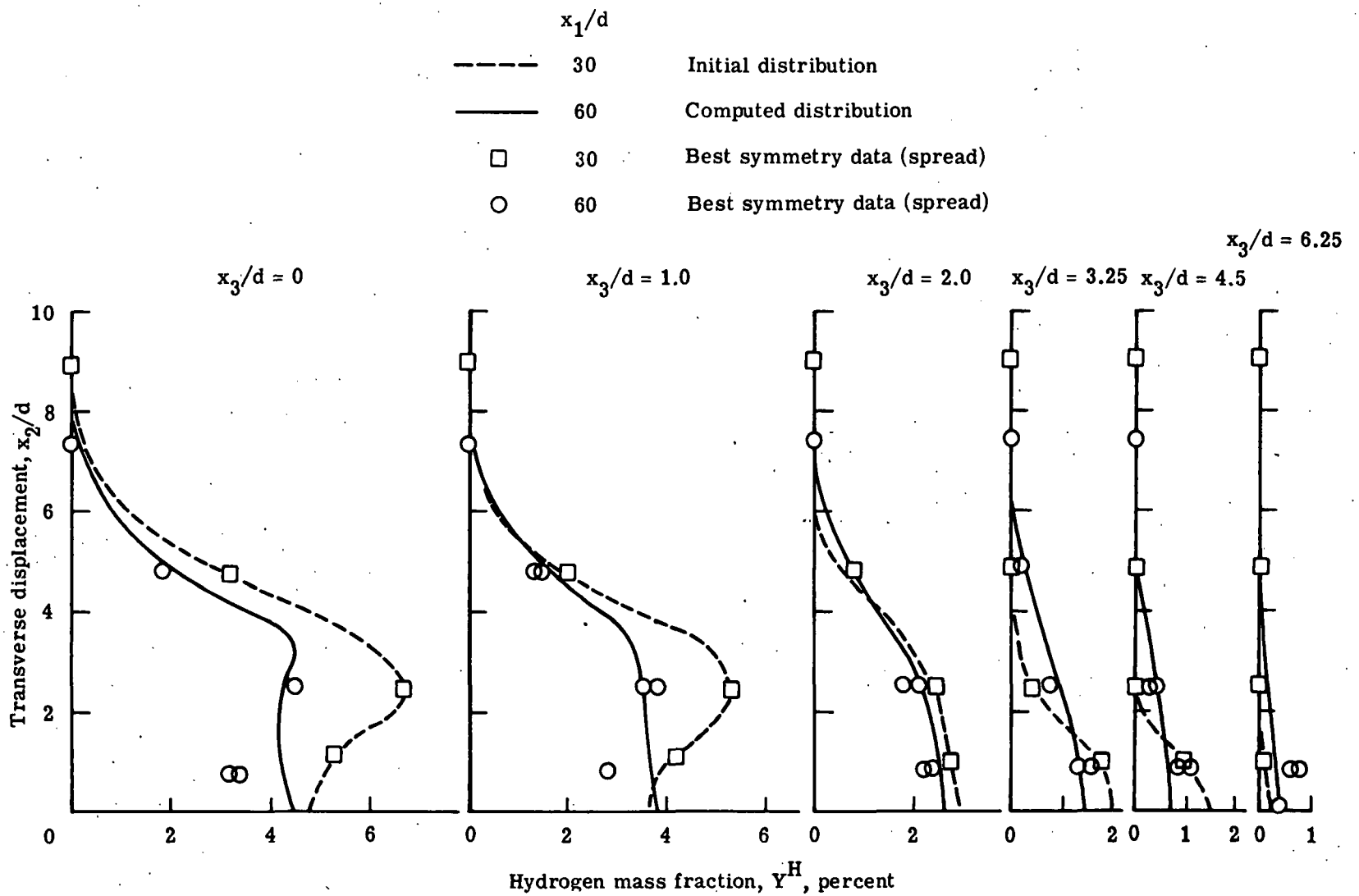

Figure 10.- Computed distribution of hydrogen mass fraction at $x_1/d = 60$.
$q_r = 1.0$; $s/d = 12.5$; $u_3 = 0$; $\lambda = 0.09$.

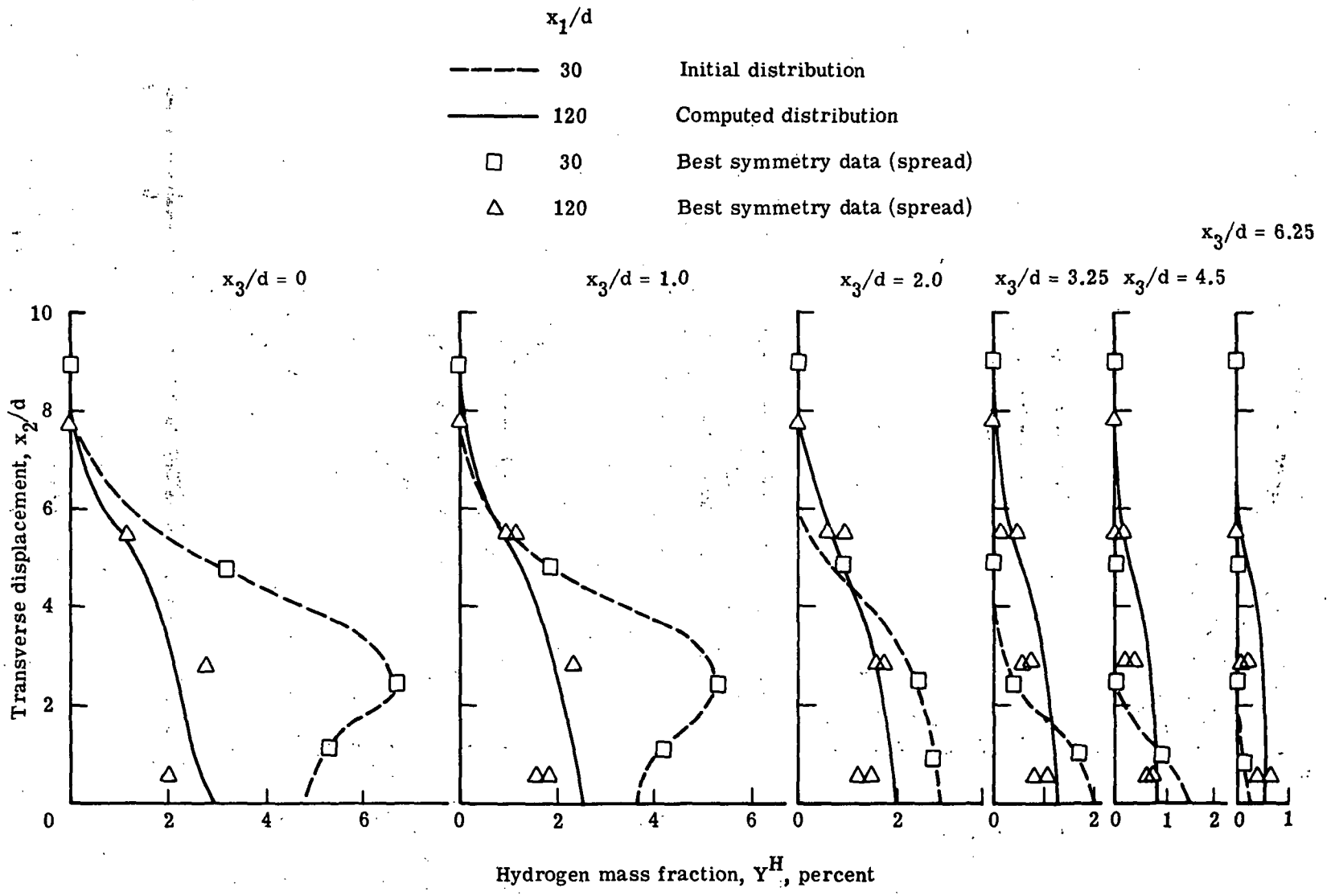

Figure 11.- Computed distribution of hydrogen mass fraction at $x_1/d = 120$.
$q_r = 1.0$; $s/d = 12.5$; $u_3 = 0$; $\lambda = 0.09$.

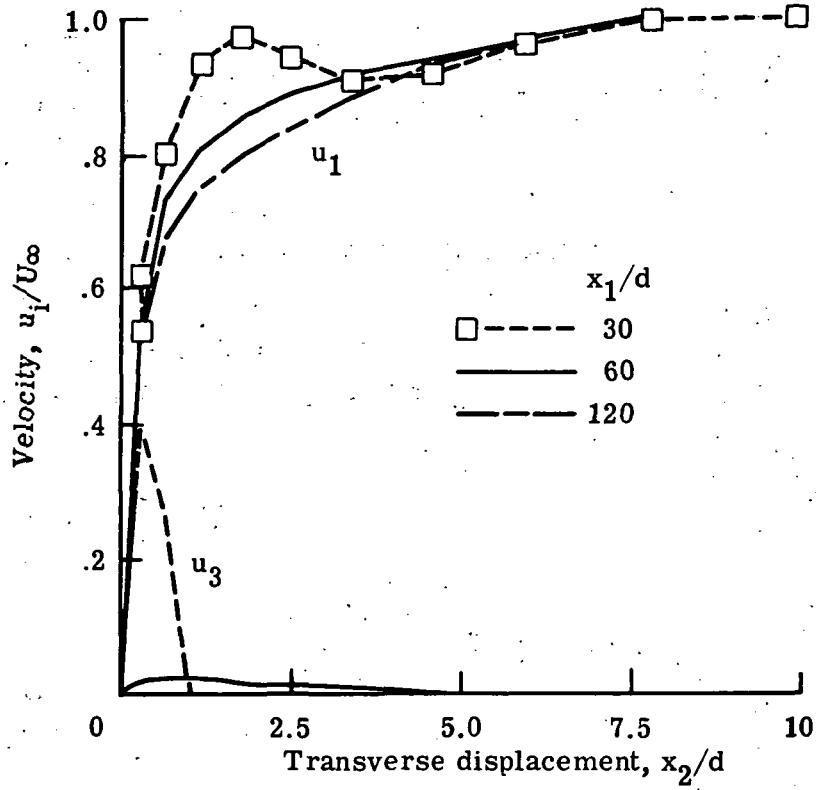

(a) Longitudinal and lateral velocities.

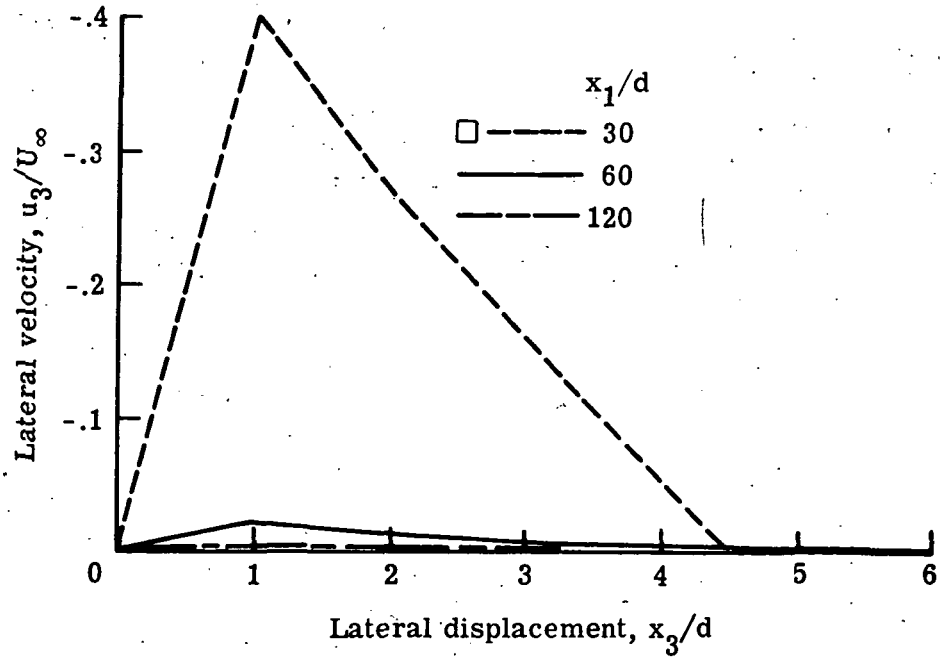

(b) Lateral velocity.

Figure 12.- Imposed transverse velocity.

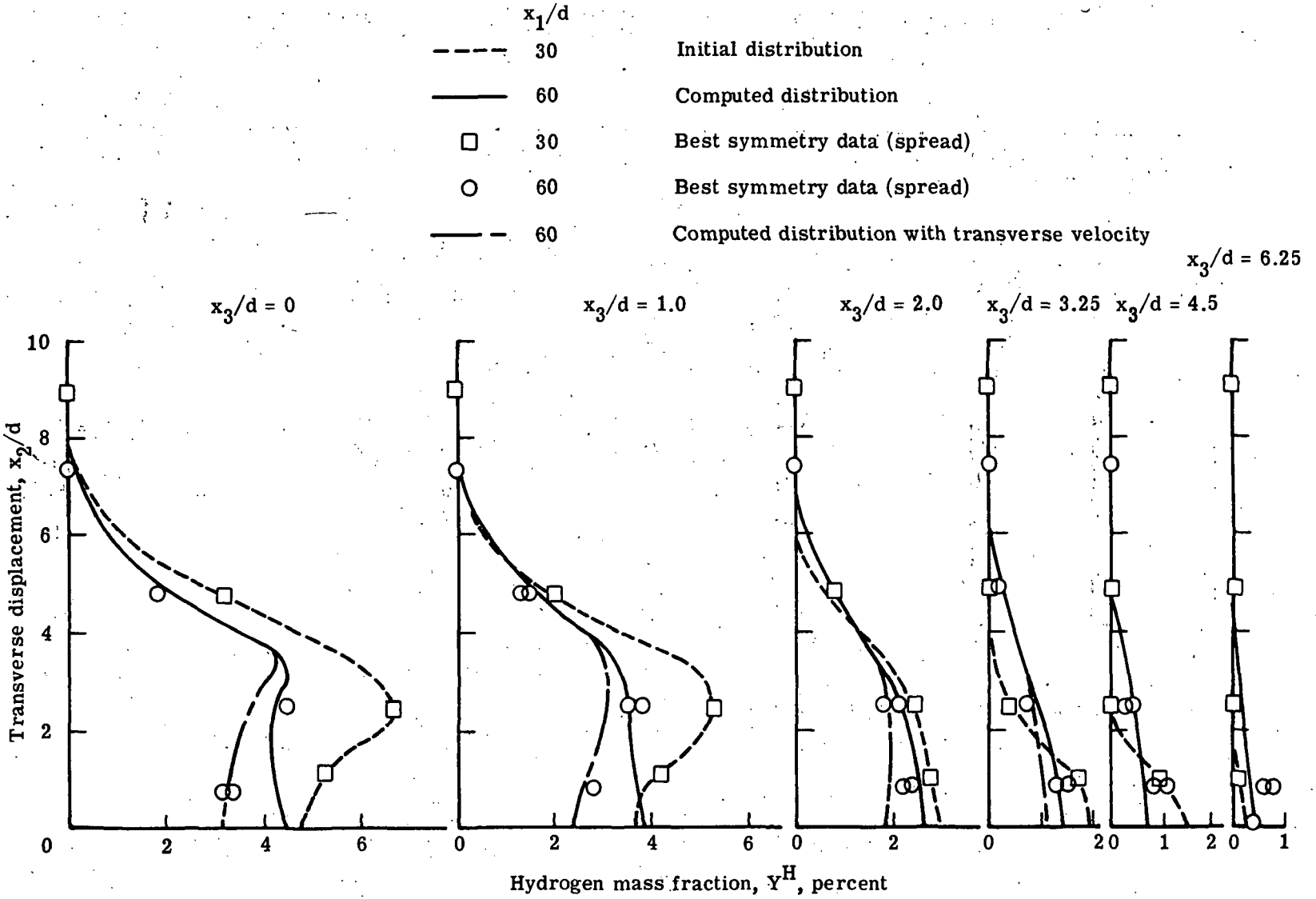

Figure 13.- Effect of transverse velocity on computed distributions of hydrogen mass fraction at $x_1/d = 60$. $q_r = 1.0$; $s/d = 12.5$; $u_3 \neq 0$; $\lambda = 0.09$.

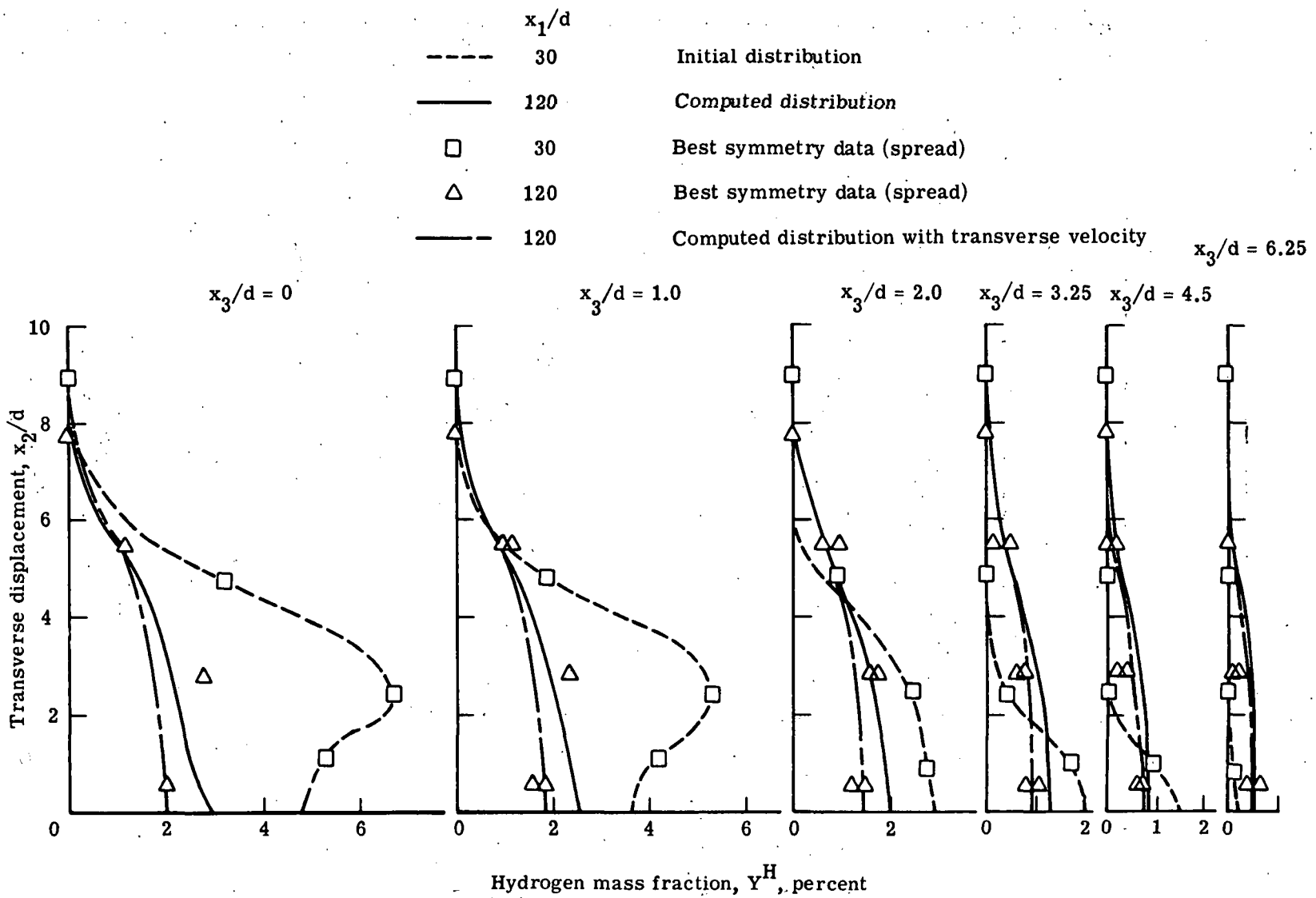

Figure 14.- Effect of transverse velocity on computed distribution of hydrogen mass fraction at $x_1/d = 120$. $q_r = 1.0$; $s/d = 12.5$; $u_3 \neq 0$; $\lambda = 0.09$.

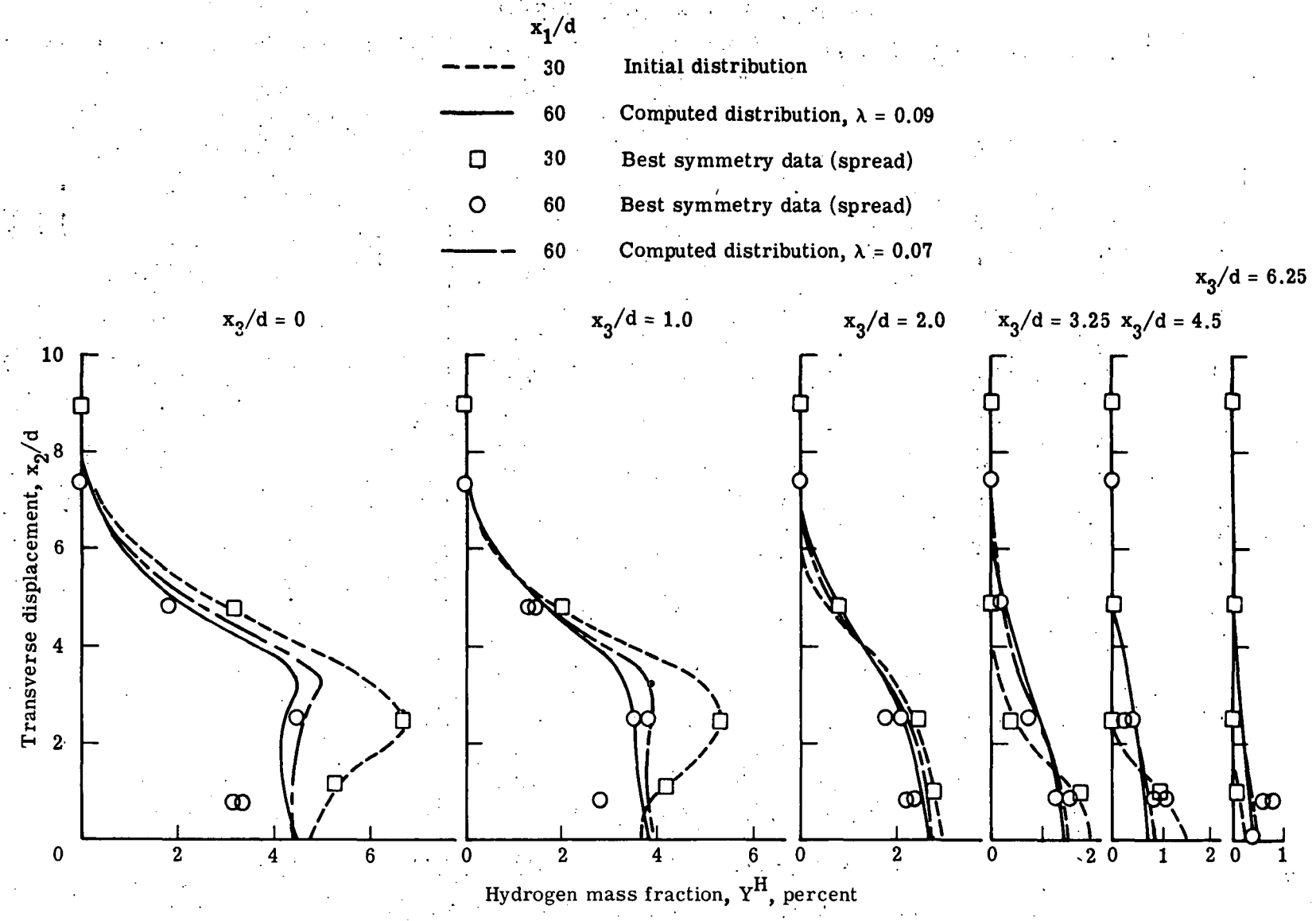

Figure 15.- Effect of turbulent sublayer constant on computed distribution of hydrogen mass fraction at $x_1/d = 60$. $q_r = 1.0$; $s/d = 12.5$; $u_3 = 0$.

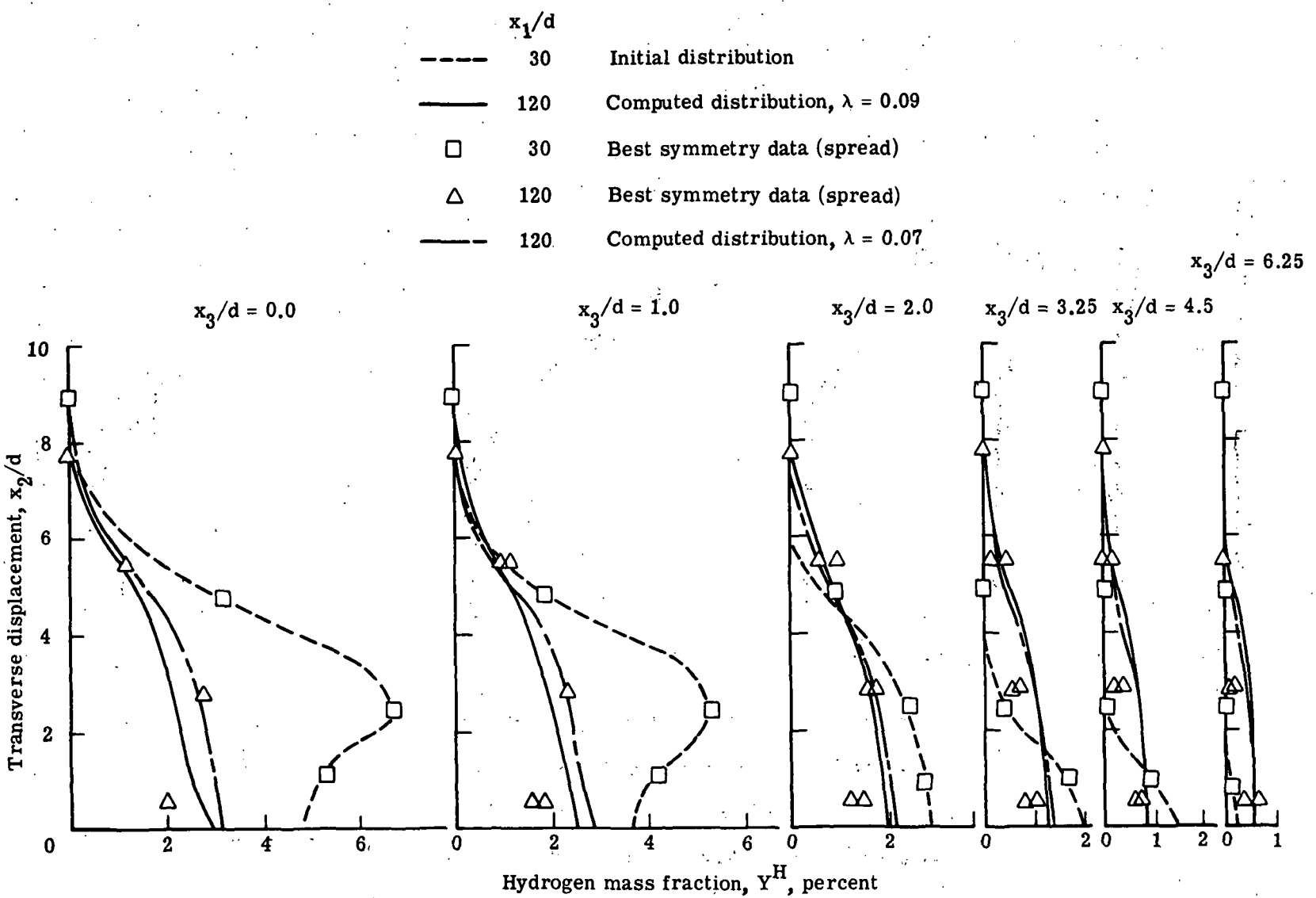

Figure 16.- Effect of turbulent sublayer constant on computed distribution of hydrogen mass fraction at $x_1/d = 120$. $q_r = 1.0$; $s/d = 12.5$; $u_3 = 0$.

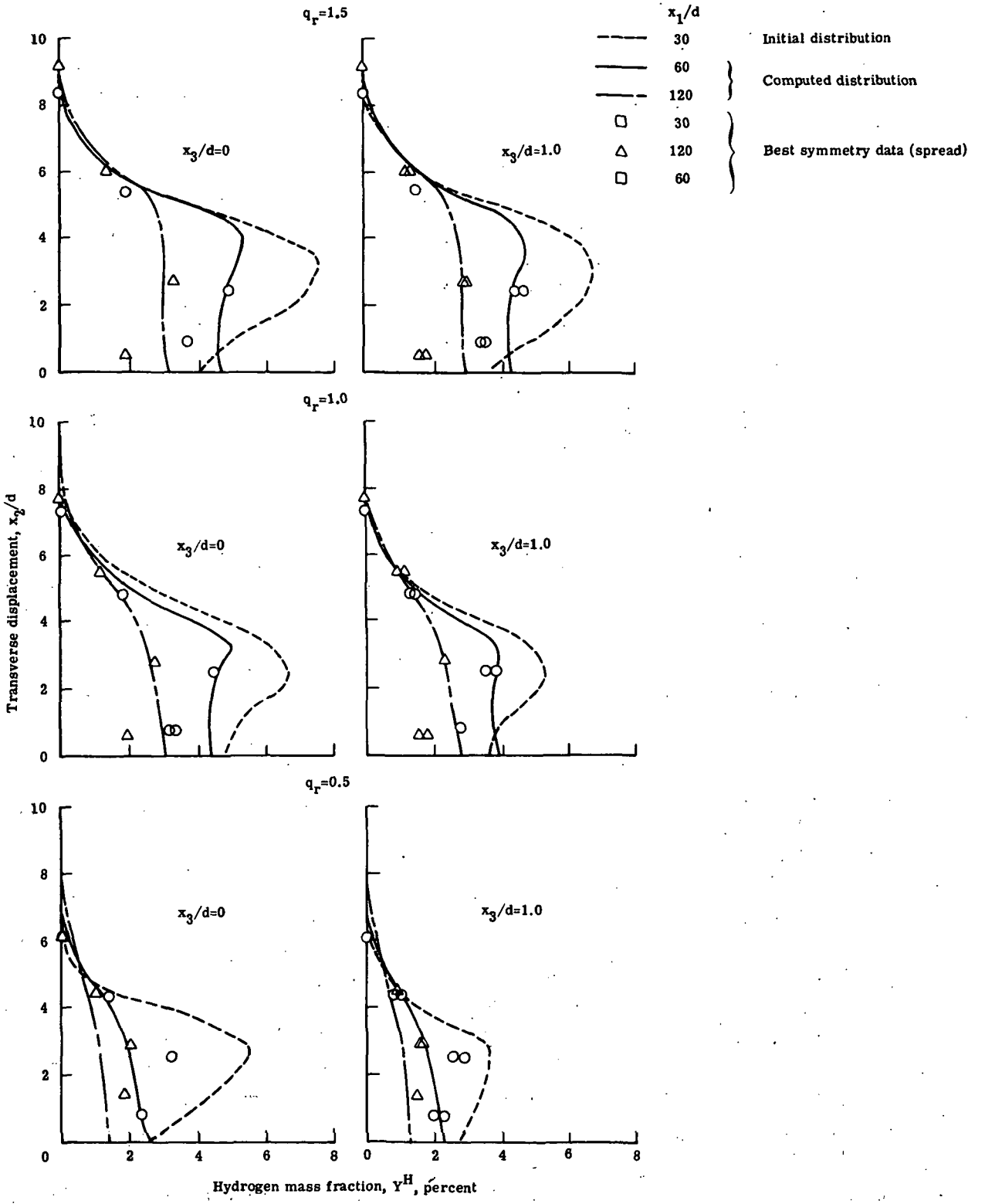

Figure 17.- Distributions of hydrogen mass fraction as a function of q_r. $s/d = 12.5$; $\lambda = 0.07$; $u_3 = 0$.

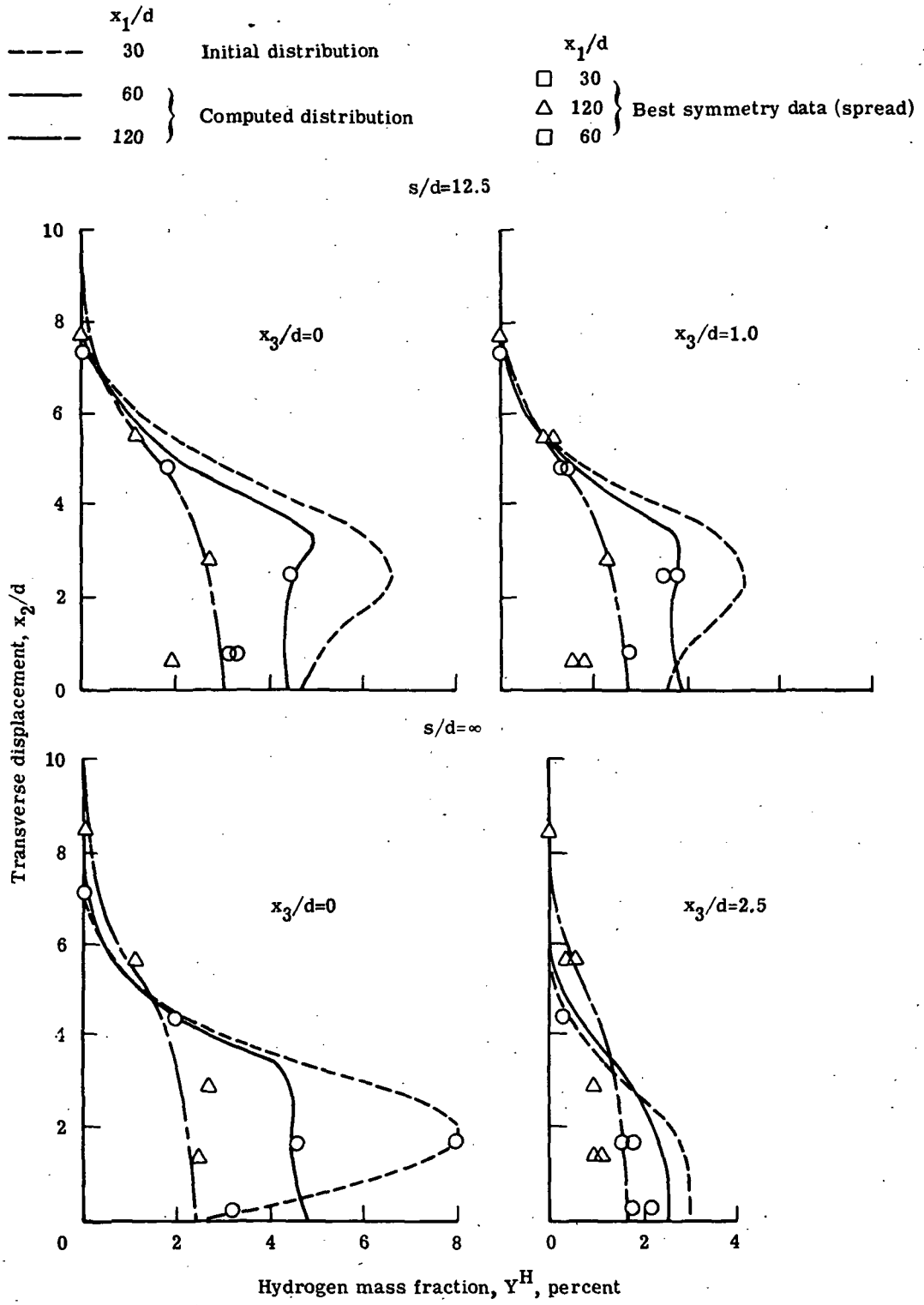

Figure 18.- Computed distribution of hydrogen mass fraction as a function of injector spacing s/d. $q_r = 1.0$; $u_3 = 0$; $\lambda = 0.07$.

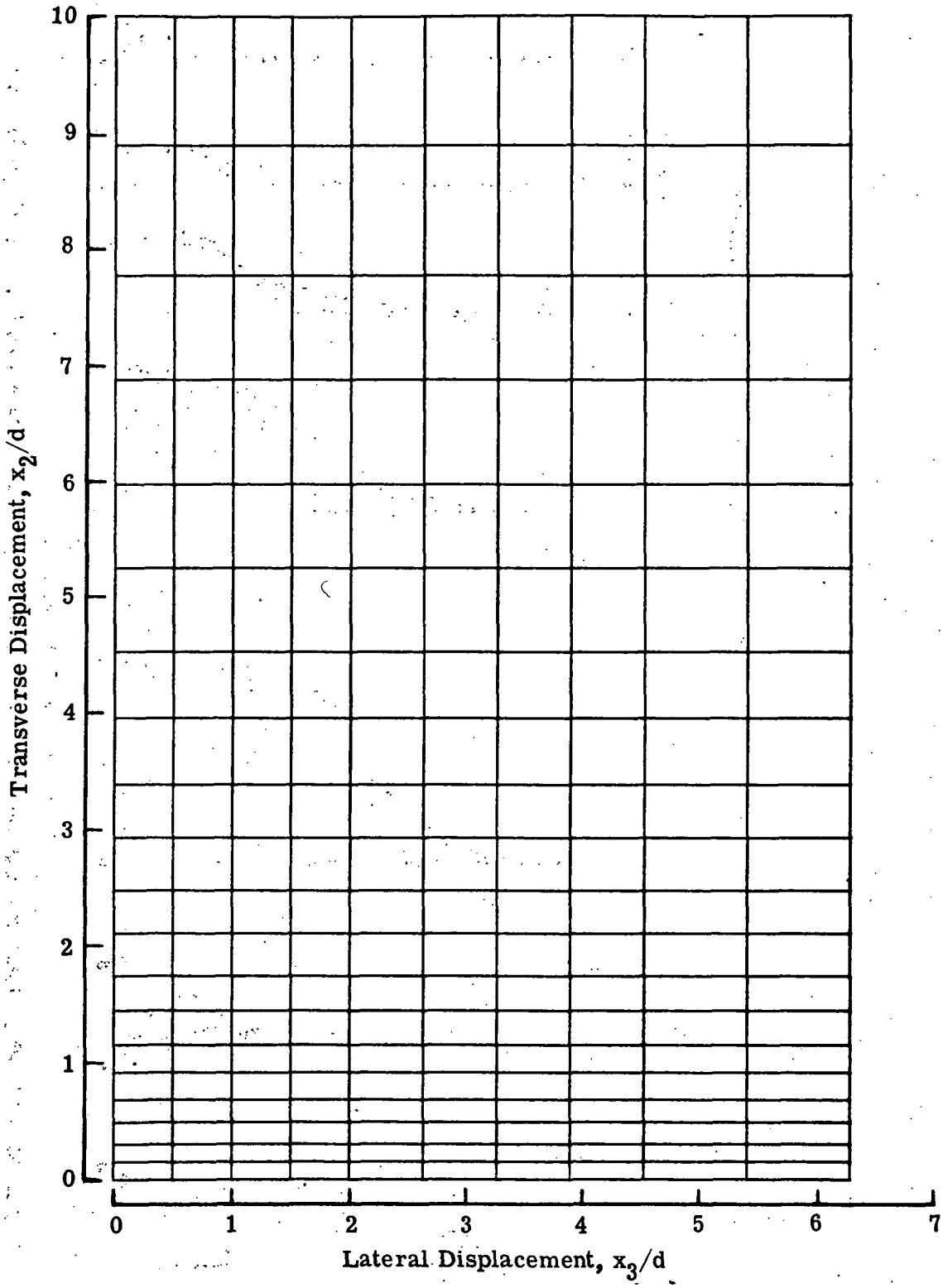

Figure 19.- Finite-element double discretization of injector solution domain.

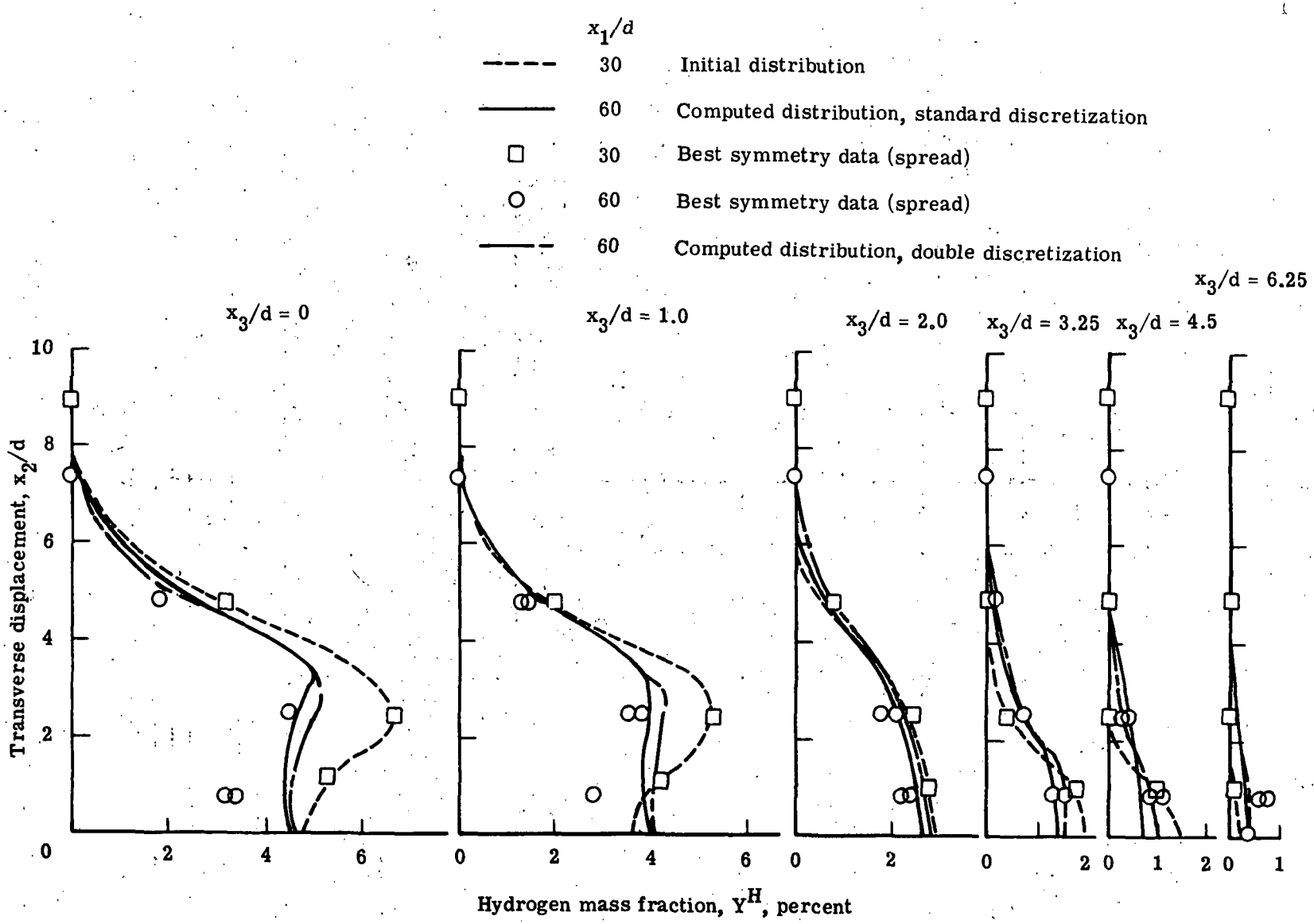

Figure 20.- Effect of discretization on computed distribution of hydrogen mass fraction at $x_1/d = 60$. $q_r = 1.0$; $s/d = 12.5$; $u_3 = 0$; $\lambda = 0.07$.

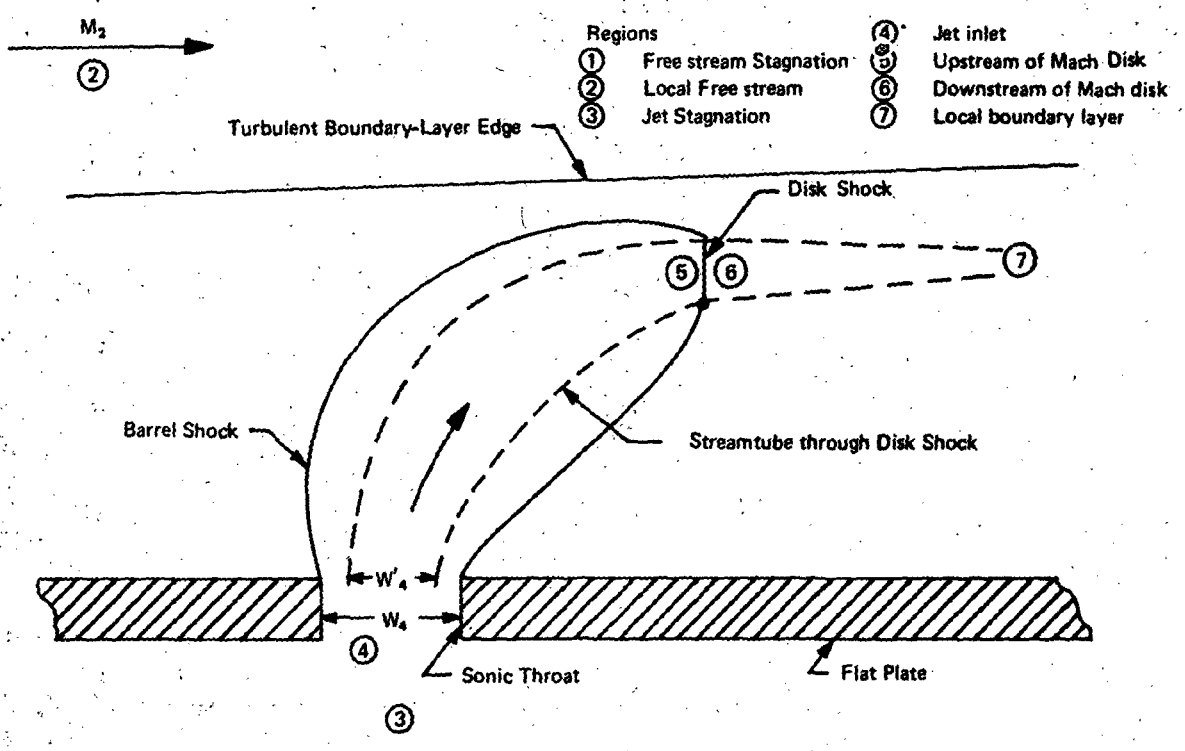

Figure 21.- Transverse injection into a turbulent boundary layer.

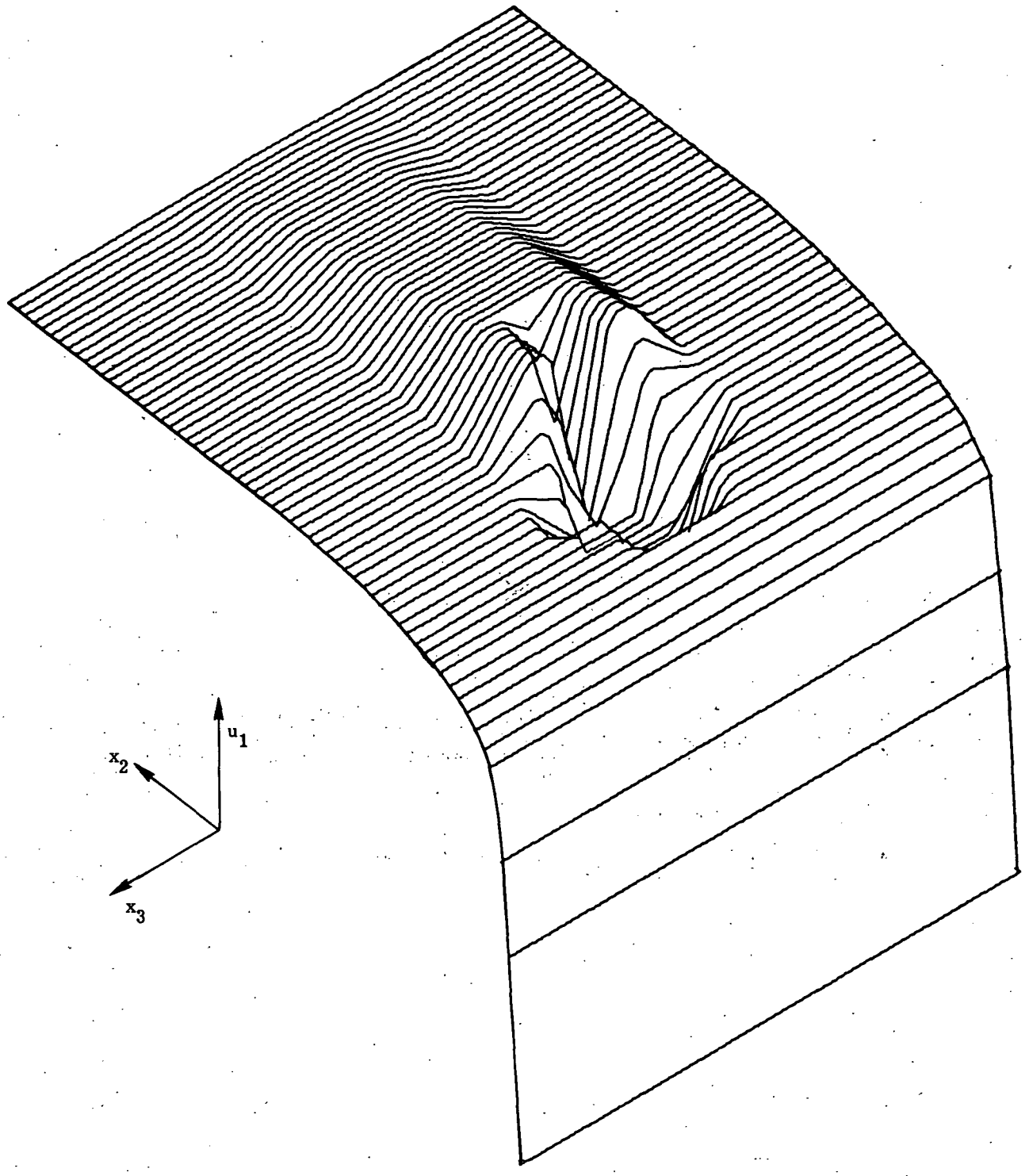

Figure 22.- Initial u_1 velocity distribution for virtual-source simulation of cold transverse hydrogen injection.

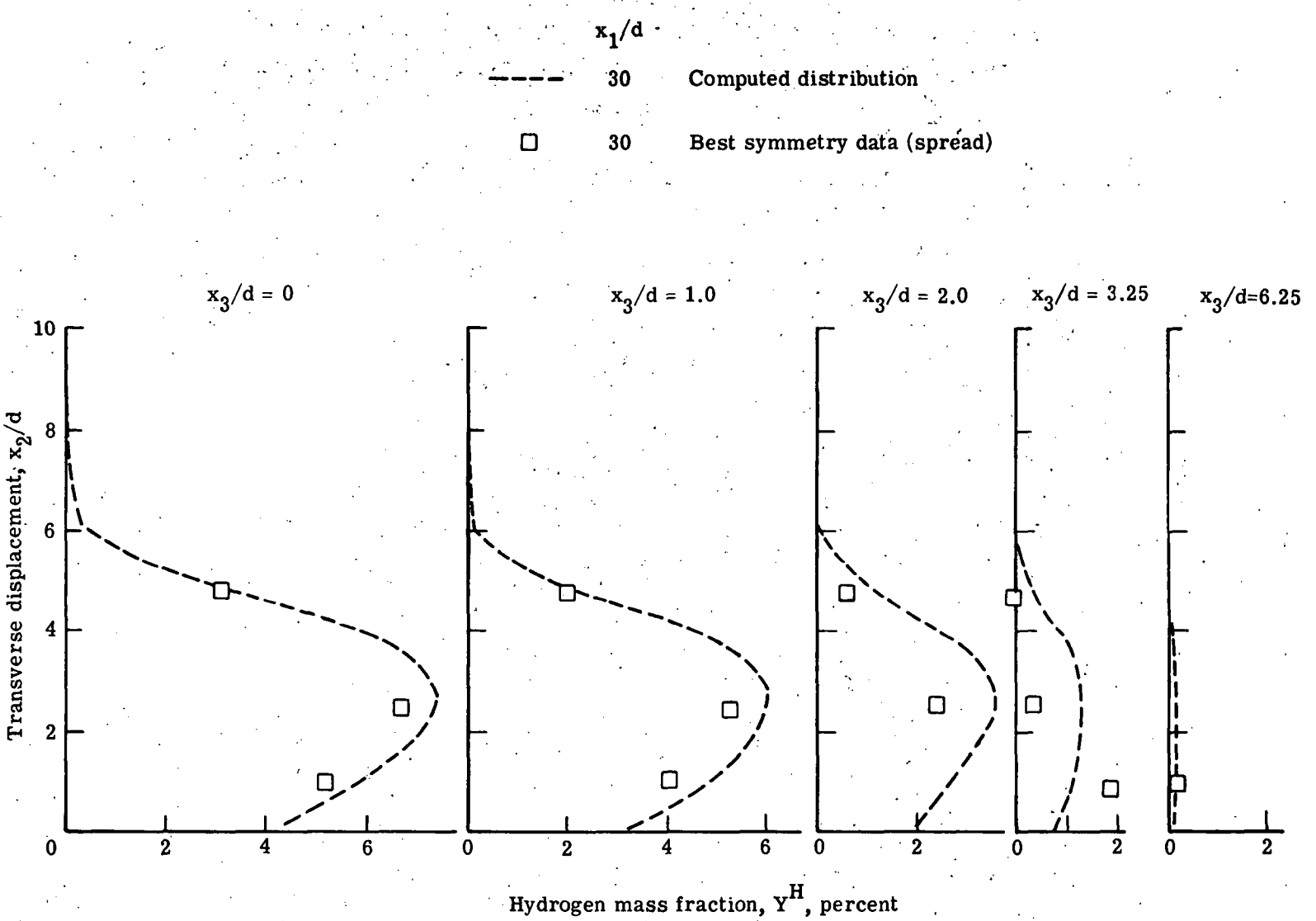

Figure 23.- Computed distributions of hydrogen mass fraction at $x_1/d = 30$ for virtual-source simulation of standard test conditions. $q_r = 1.0$; $s/d = 12.5$; $u_3 = 0$; $\lambda = 0.07$.

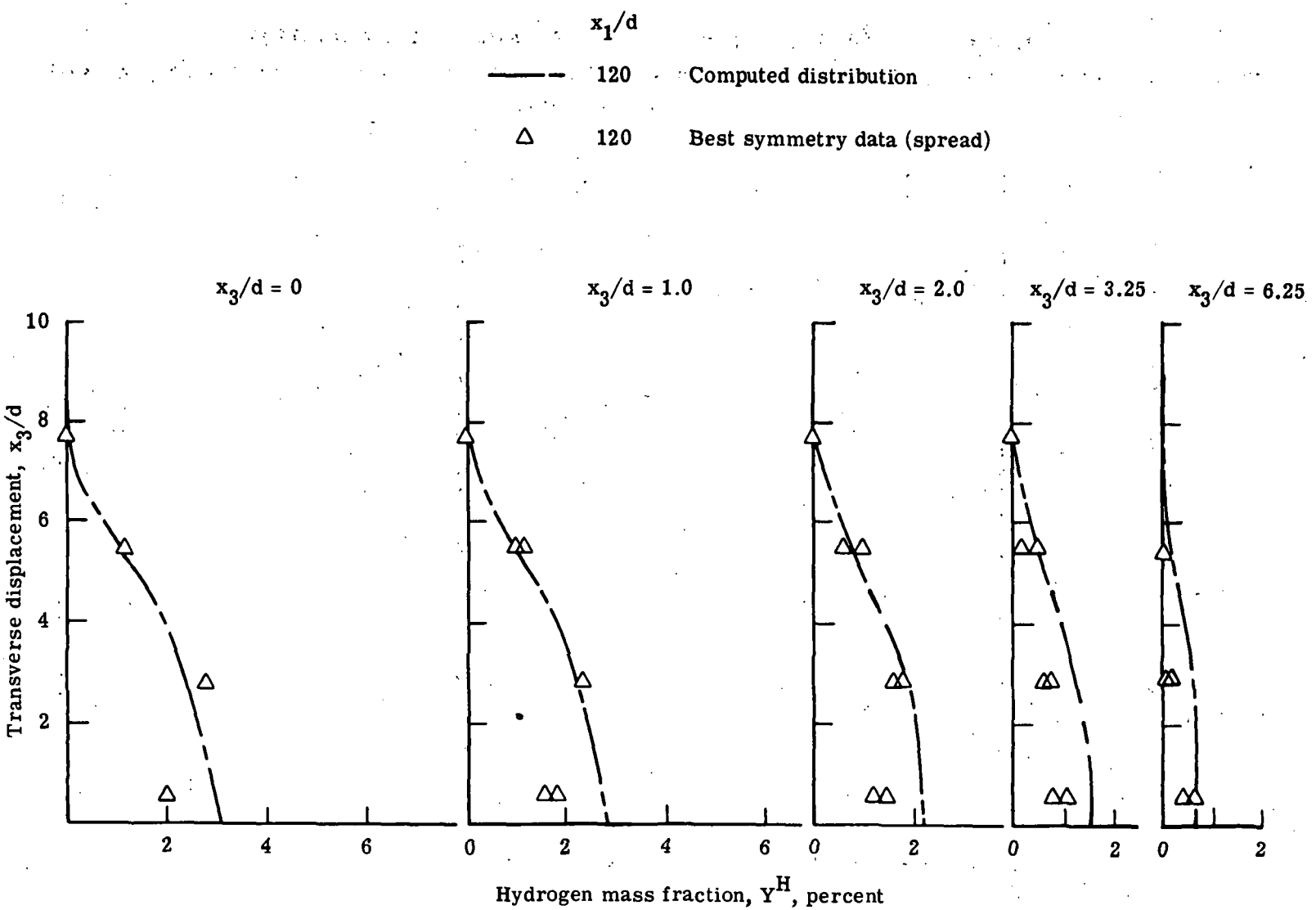

Figure 24.- Computed distribution of hydrogen mass fraction at $x_1/d = 120$ for virtual-source simulation of standard test conditions. $q_r = 1.0$; $s/d = 12.5$; $u_3 = 0$; $\lambda = 0.07$.

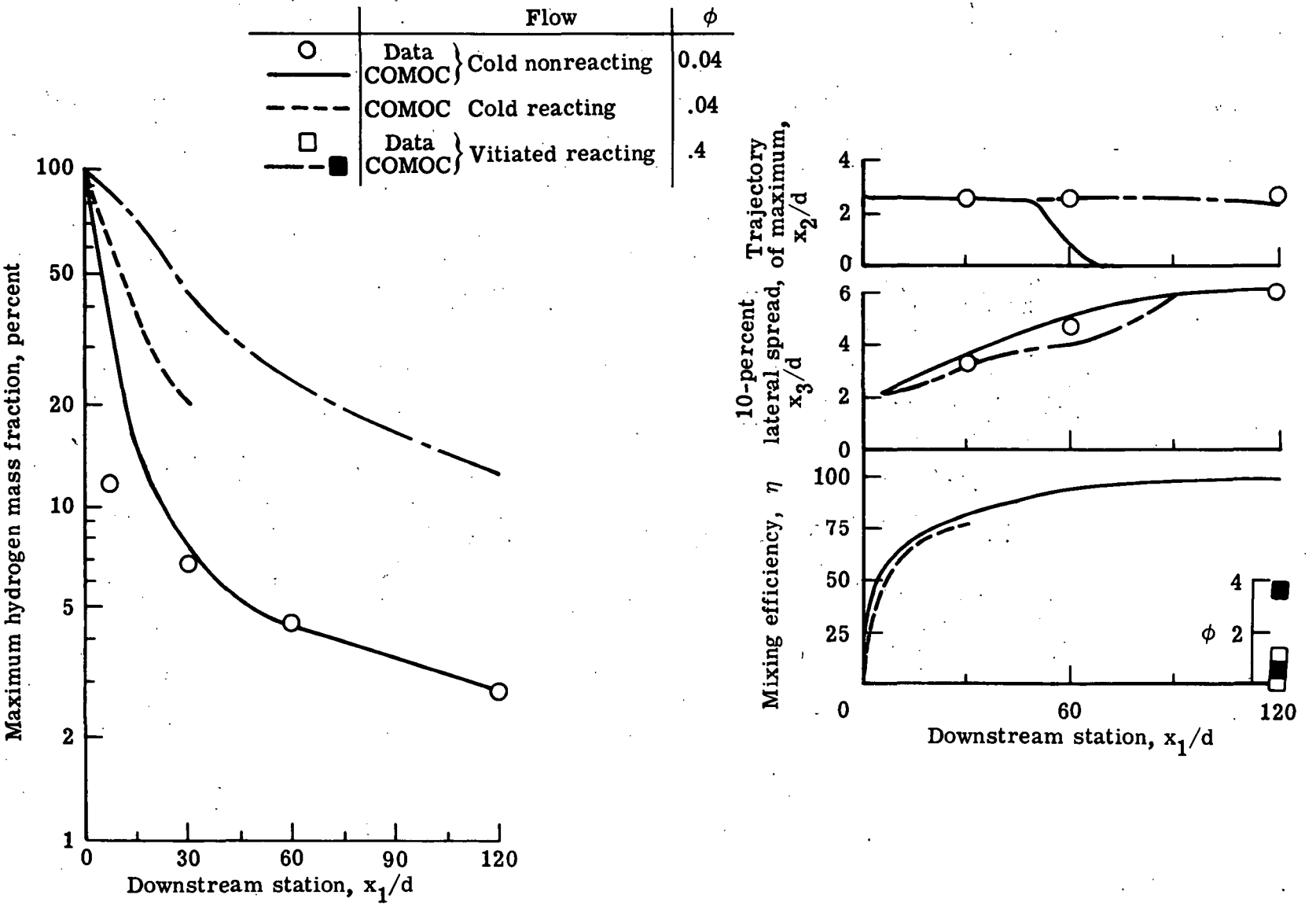

Figure 25.- Transverse cold hydrogen injection – virtual-source simulation. $q_r = 1.0$; $s/d = 12.5$.

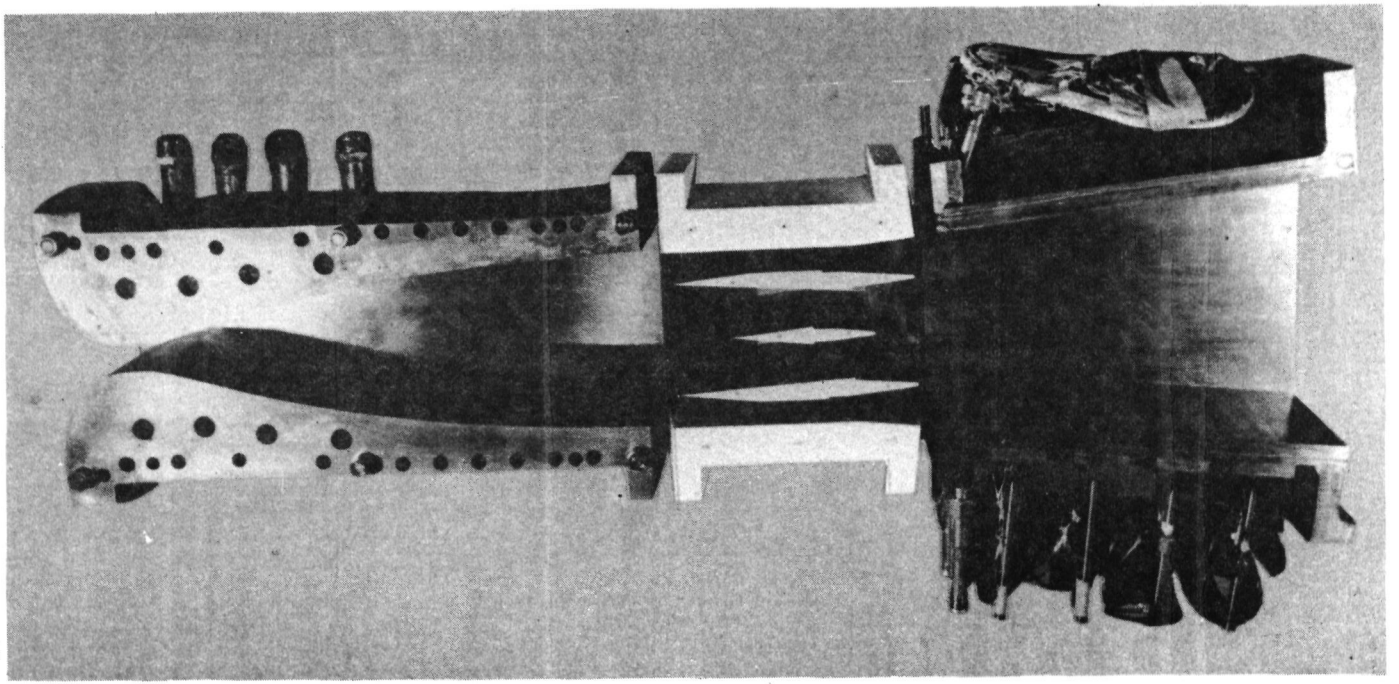

Figure 26.- Scramjet combustor model.

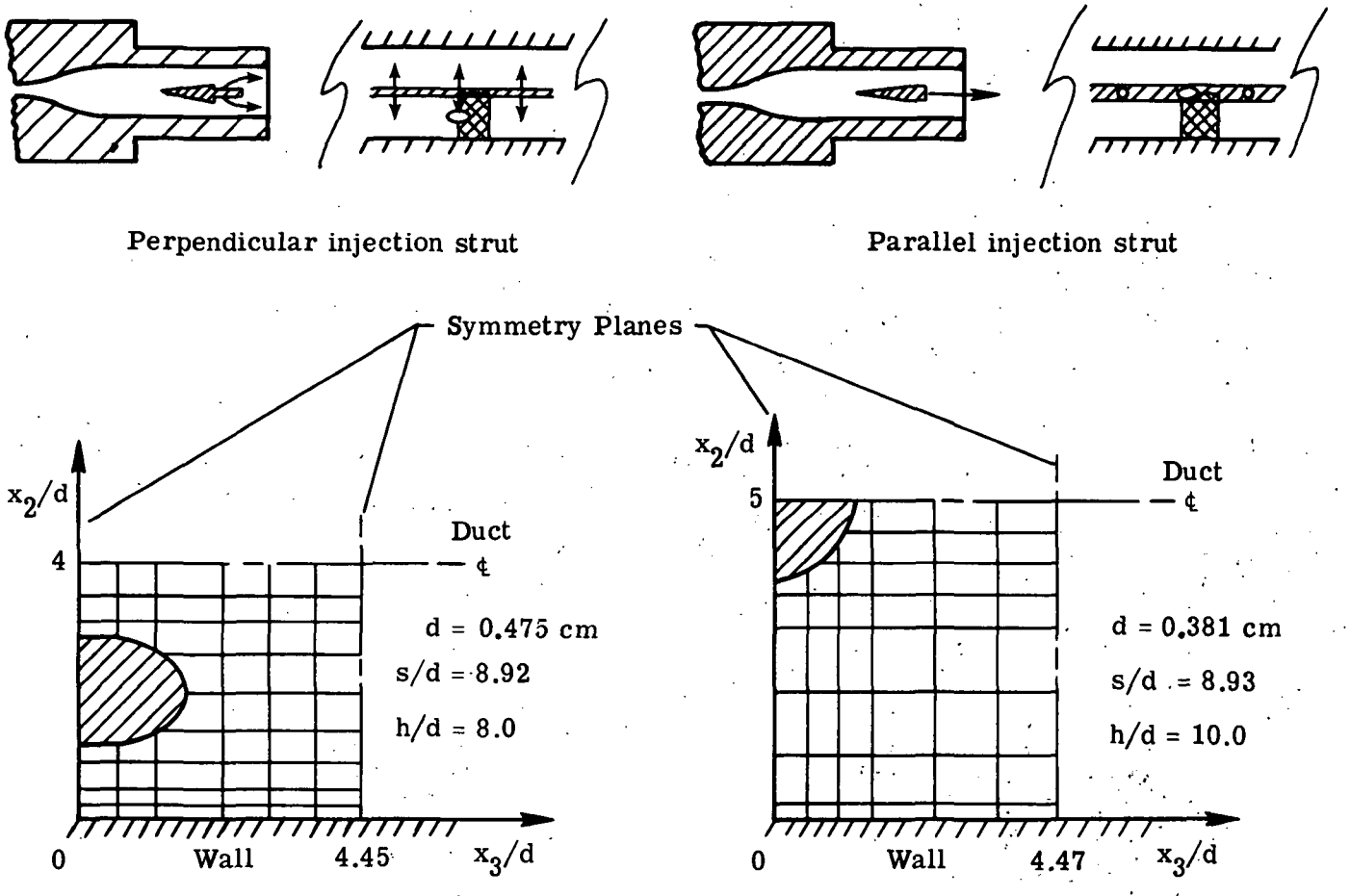

Figure 27.- Two fuel injector struts (ref. 11) for supersonic combustion, with virtual-source simulation.

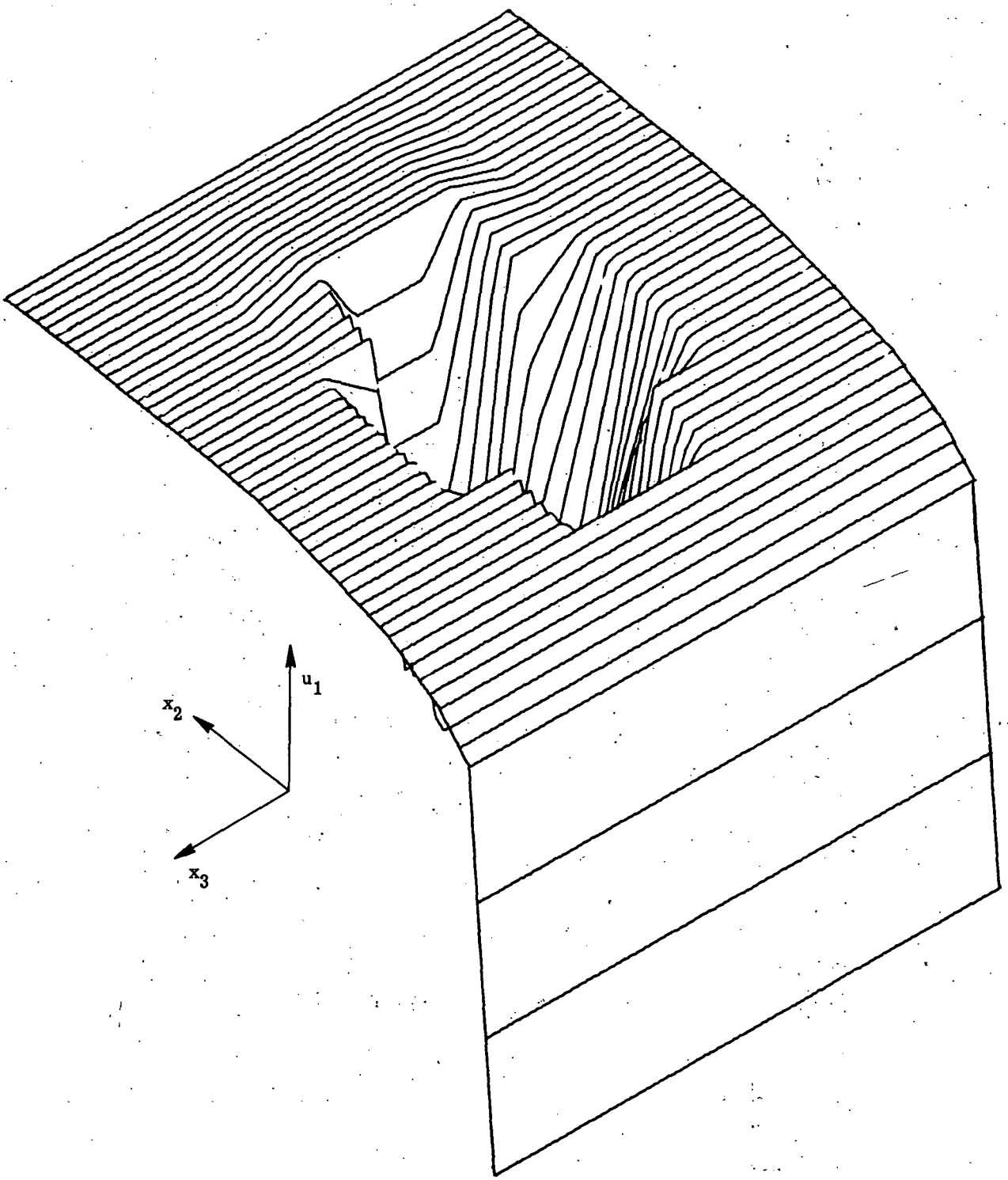

(a) $x_1/d = 0.$

Figure 28.- Longitudinal velocity distributions from virtual-source simulation of perpendicular injector.

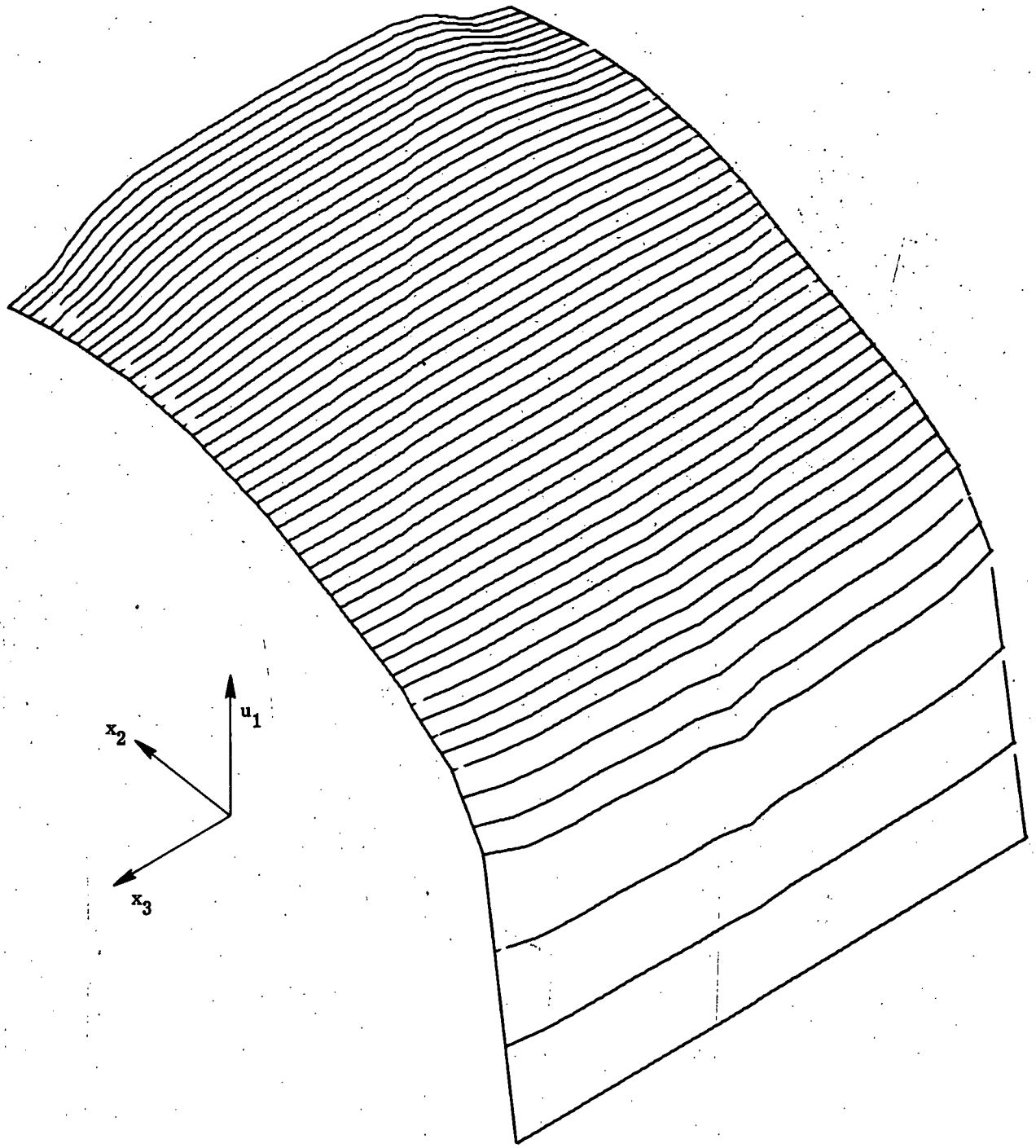

(b) $x_1/d = 150.$

Figure 28. - Concluded.

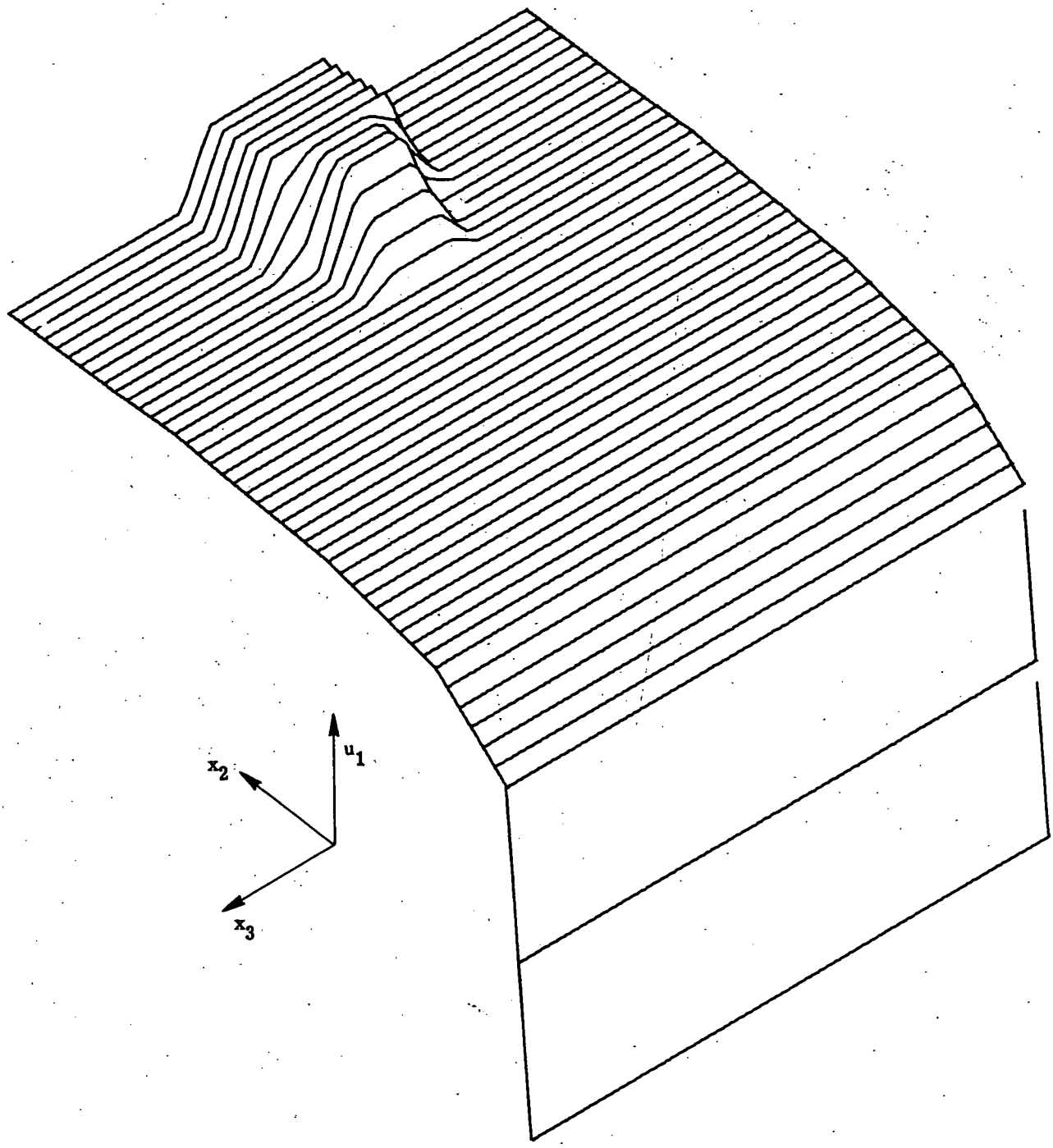

(a) $x_1/d = 0.$

Figure 29.- Longitudinal velocity distributions from virtual-source simulation of parallel injector.

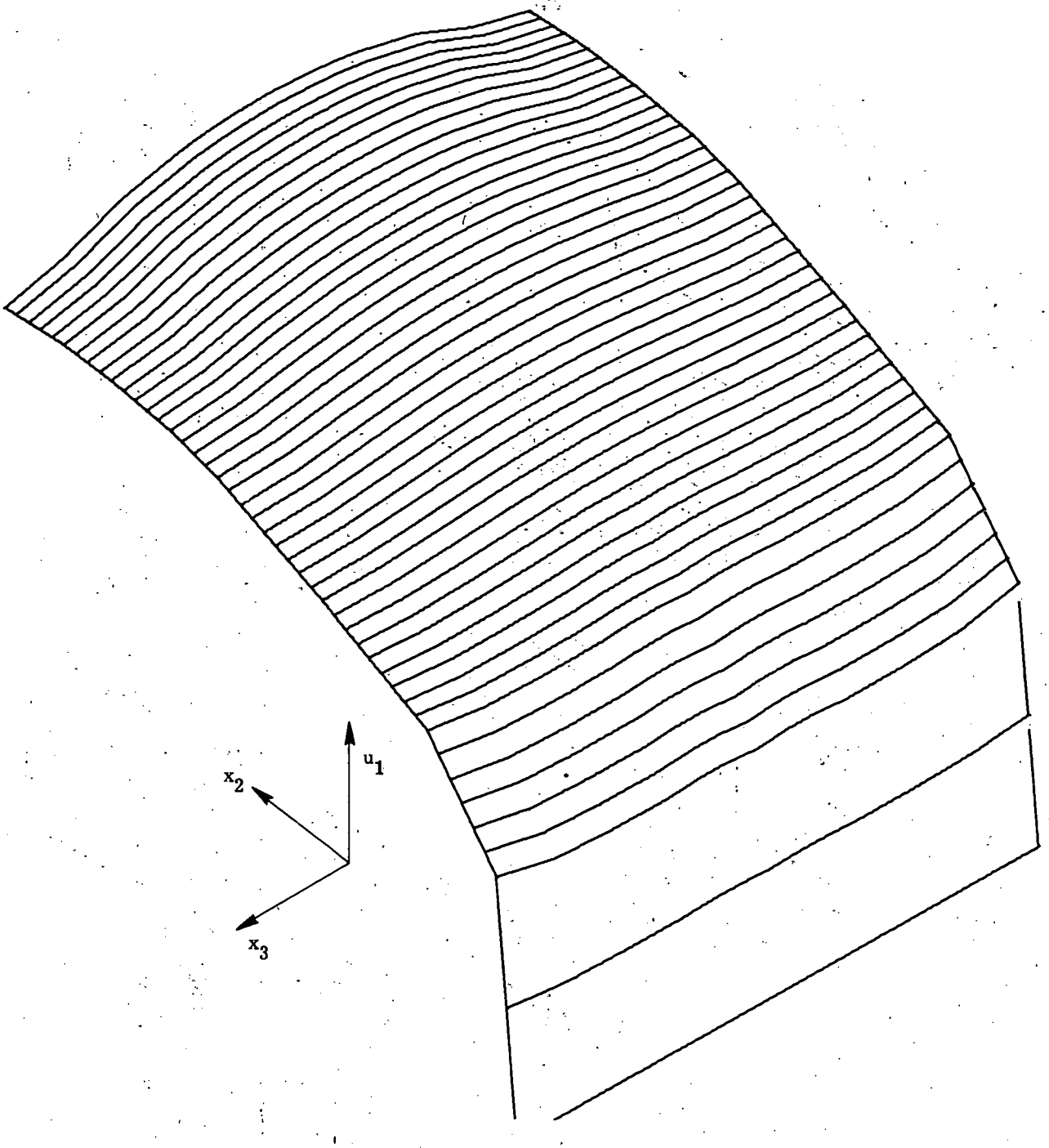

(b) $x_1/d = 150.$

Figure 29.- Concluded.

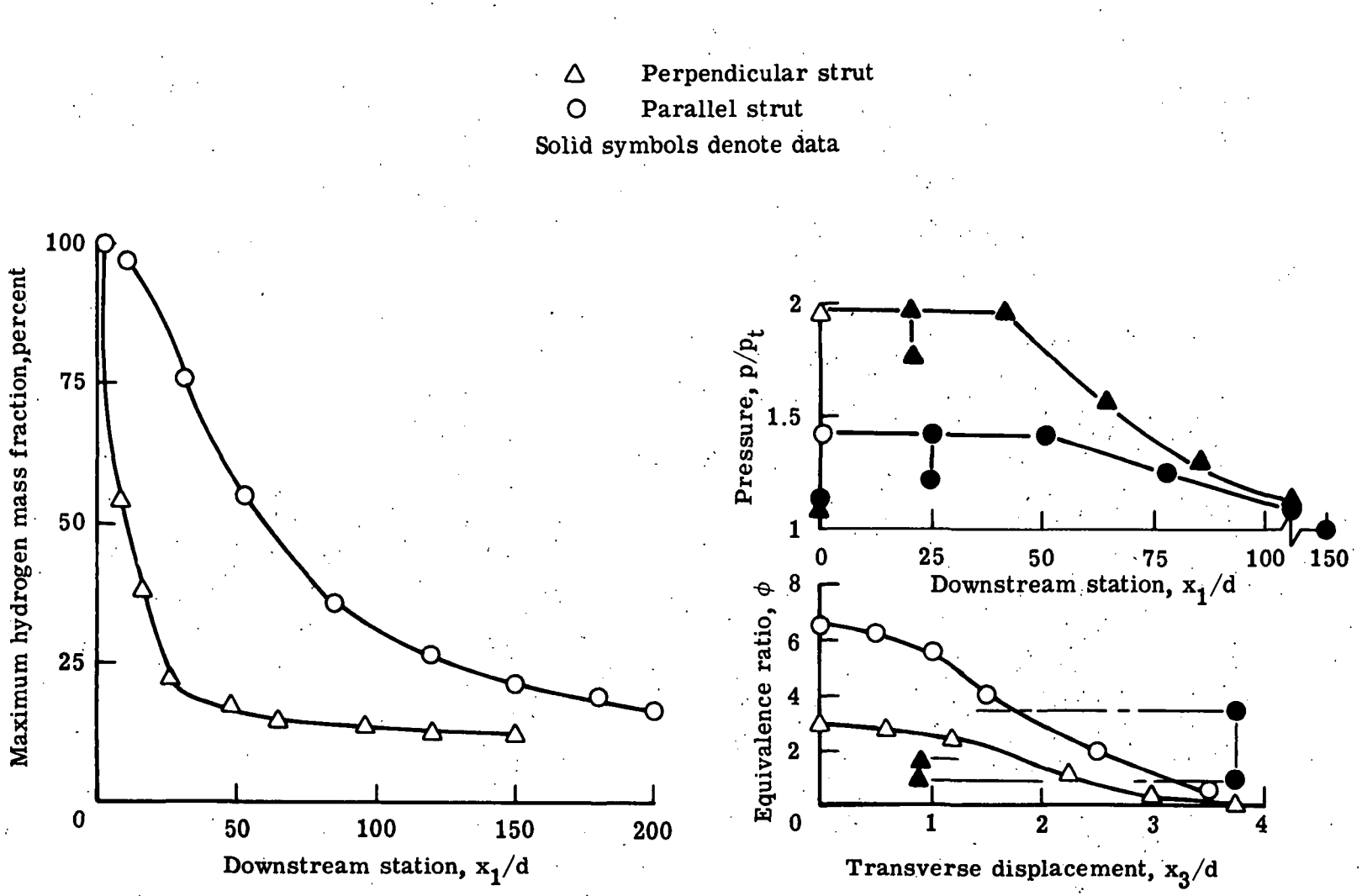

Figure 30.- Analytical evaluation of two supersonic strut injectors from virtual-source simulation. M = 3; ϕ = 0.6; s/d = 9.